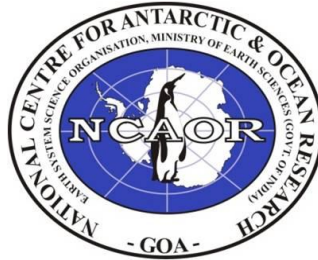


Temporal variations in Velocity of the Amery Ice shelf System, East Antarctica



National Centre for Antarctic and Ocean Research
Polar Remote Sensing Division

Under the guidance of

Dr. Shridhar D. Jawak
Dr. Alvarinho J. Luis

Work carried out by

Adithi R. Upadhya

MSc. Geoinformatics
Bharati Vidyapeeth Institute of Environment Education and Research

2018

Acknowledgement

I would take this opportunity to thank all the people who in some way or the other have contributed to complete my internship.

First and foremost, I would like to thank my guide Dr. Shridhar D. Jawak, for his guidance and complete support all the time. His clear vision of the project was the only thing that kept me motivated throughout the project. His evening walks will always be remembered.

I would like to thank Dr. Alvarinho J.Luis, Head of Polar Remote Sensing Division for selecting my application for the internship.

I would like to express my sincere gratitude to Dr. Erach Barucha, Dr. Shamita Kumar, Dr. Kranti Yardi, and Mrs. Prachi Dev for their constant support and encouragement to pursue internship at NCAOR, Goa.

I would like to convey my gratitude to Mrs. Neelu Singh whose presence completely filled the gap of a guardian and an elder sister. I would specially like to thank Ms. Mansi Joshi, Ms. Vigna Purohit, Ms. Sravanthi Mopati, Ms. Deepthi R, Mr. Utkarsh Khot, Mr. Shubhang, and Mr. Bikash for being the way they are and constantly helping me. Last but not the least; I would like to thank my lab mates Mr. Kirti Mahanta, Mr. Mahfooz Alam and Mr. Varkichan Joy, Mr. Sagar Wankhede.. I would like to thank my college friends for always cheering me up.

Finally I would like to thank my friends and family. I would like to thank my dance class Kalavardhini and brother (Abhijith) for their mere presence kept my body and soul calm. A special thanks to Mrs. Medha and family, for providing accommodation along with lots of love. Also, Milky (our pet) will never be forgotten.

Table of Contents

1. Introduction.....	6
1. Glaciers.....	6
2. Valley glaciers.....	6
3. Tidewater glaciers.....	6
2. Objective.....	8
3. Study Area.....	8
4. Background.....	9
4.1 SAR Interferometry.....	9
4.2 Offset Tracking.....	12
4.3 Optical Feature Tracking.....	13
5. Data set.....	16
6. Software's Used.....	21
7. Methodology.....	22
1. BIA Extraction.....	22
2. Melt Duration Estimation:.....	24
3. Velocity Derivation (SAR Images).....	25
4. Velocity Derivation (Optical Images).....	29
8. Stable Dataset Generation.....	33
9. Results.....	34
9.1. Velocity.....	34
9.2. Blue Ice Areas.....	38
9.3. Melt.....	38
9.4. Elevation.....	39
10. Analysis.....	40
10.1. Slope.....	40
10.2. Velocity Analysis.....	41
10.3. BIA Analysis.....	42
10.4. Elevation Analysis.....	43
11. Discussion.....	45
12. Work and Cultural Experience.....	50

13. References	51
----------------------	----

Table of Figures

Figure 1: Regions covered with Glaciers.....	6
Figure 2: Study Area.....	9
Figure 3: SAR Interferometry Principle	11
Figure 4: Methods used for Velocity Estimation.....	16
Figure 5: Sentinel 1A and B characteristics.....	18
Figure 6: Landsat 7 and 8 characteristics.....	21
Figure 7: Apply Orbit File	25
Figure 8: Dem Assisted Coregistration.....	26
Figure 9: Offset tracking.....	26
Figure 10: Terrain Correction	27
Figure 11: Correlation.....	30
Figure 12: Frequency parameters.....	31
Figure 13: Stable Dataset generated	33
Figure 14: MEaSURES 450m	34
Figure 15: Yearly velocity maps generated	37
Figure 16: Monthly velocity maps generated	37
Figure 17: Blue Ice Area velocity.....	38
Figure 18: Melt Duration	39
Figure 20: Elevation Distribution	40
Figure 21: Slope Derived From Velocity.....	40
Figure 22: Bias with respect to MEaSURES 450 m.....	41
Figure 23: RMSE with respect to MEaSURES 450 m.....	41
Figure 24: Correlation with respect to MEaSURES 450 m.....	42
Figure 25: Bias of BIA's with respect to MEaSURES 450 m	42
Figure 26: RMSE of BIA's with respect to MEaSURES 450 m	43

Figure 27: Correlation of BIA's with respect to MEaSURES 450 m 43
Figure 28: Bias of BIA's with respect to MEaSURES 450 m 44

1. Introduction

1. Glaciers

Glaciers are made up of fallen snow that, over many years, compresses into large, thickened ice masses. Glaciers form when snow remains in one location long enough to transform into ice. Due to sheer mass, glaciers flow like very slow rivers.

A glacier is a slowly flowing mass of ice with incredible erosive capabilities. Valley glaciers (alpine glaciers, mountain glaciers) excel at sculpting mountains into jagged ridges, peaks, and deep U-shaped valleys as these highly erosive rivers of ice progress down mountainous slopes.

Presently, glaciers occupy about 10 percent of the world's total land area, with most located in Polar Regions like Antarctica, Greenland, and the Canadian Arctic. Glaciers can be thought of as remnants from the last Ice Age, when ice covered nearly 32 percent of the land, and 30 percent of the oceans. Most glaciers lie within mountain ranges that show evidence of a much greater extent during the ice ages of the past two million years, and more recent indications of retreat in the past few centuries.



Figure 1: Regions covered with Glaciers

1.1 Types of Glaciers

1. Mountain Glaciers

These glaciers develop in high mountainous regions, often flowing out of ice-fields that span several peaks or even a mountain range. The largest mountain glaciers are found in Arctic Canada, Alaska, the Andes in South America, and the Himalaya in Asia.

2. Valley glaciers

Commonly originating from mountain glaciers or ice-fields, these glaciers spill down valleys, looking much like giant tongues. Valley glaciers may be very long, often flowing down beyond the snow line, sometimes reaching sea level.

3. Tidewater glaciers

As the name implies, these are valley glaciers that flow far enough to reach out into the sea. Tidewater glaciers are responsible for calving numerous small icebergs, which although not as imposing as Antarctic icebergs, can still pose problems for shipping lanes.

1.2 Glacier Flow

A glacier begins to flow when a thick mass of ice begins to deform plastically under its own weight. This process of plastic deformation (internal deformation) occurs because the ice crystals are able to slowly bend and change shape without breaking or cracking. Plastic deformation occurs below a depth of 50 meters (164 feet) from the surface of the glacier.

Thick glacial ice is quite heavy, and the great weight of the glacier may cause the ice along the base of the glacier to melt. Melting occurs because the temperature at which ice melts is reduced due to the pressure exerted by the weight of the overlying glacial ice. Heat from the Earth's surface may also cause ice to melt along the base of the glacier. The process of basal sliding occurs when a thin layer of melt water accumulates between the basal ice and the Earth's surface. The melt water functions as a lubricant allowing the glacier to slide more readily over bedrock and sediments.

1.3 Microwave remote sensing of Glaciers

Interferometry has enabled to exploit the phase difference of the acquired signal to find the displacement. In the interferometric approach, two complex SAR images acquired from slightly different orbit configurations and at different times are combined to give interferograms. The interferometric phase is sensitive to both surface topography and coherent displacement along the look vector occurring between the acquisitions of the interferometric image pair. D-InSAR, Differential Interferometric Synthetic Aperture Radar is used for removal of topographic phase from interferogram. But the main drawback is temporal decorrelation.

Another method is speckle tracking where speckle in SAR images are traced in pair of image master and slave for identifying features which have been displaced. Speckle is a scattering phenomenon since the resolution is not sufficient enough for the scatterers. Speckle tracking exploits the offsets in range and azimuth while being ignorant of phase. It is usually used for high velocity glaciers and also for long repeat cycle. The algorithm used is the complex cross correlation between the pair of images to track motion of surface. Tie points are generated by matching speckle portion between images just like in co-registration and then they are calibrated to calculate surface motion. The main requirement in this process is the pair of images from the same track having the same look and incidence angle, in simple terms of the same path and frame for co registration.

In addition to passively sensing emissions coming from objects on Earth, satellite sensors can also *actively* emit microwaves toward the earth's surface. These microwaves reflect off the surface and return to the sensors. This type of remote sensing is called active microwave, or radar. This same technology is used to track aircraft, ships, and speeding automobiles. As with

passive microwave energy, the physical properties of objects at the earth's surface determine the amount and characteristics of microwave radiation bounced back to the sensor.

1. Imaging radar

Imaging radar is similar to a photograph taken by a camera, but the image is of radar waves, not visible light. In general, though, thicker multiyear ice is readily distinguishable from younger, thinner ice because radar energy bounces back to the sensor from the bubbles in the ice left when brine drains. SAR is a special type of imaging radar that involves advanced technology and complex data processing to obtain detailed images of sea ice. The RADARSAT mission, managed by the Canadian Space Agency, is the primary SAR mission today. This fine resolution allows them to analyze sea ice and help route ships through ice-covered regions. SAR imagery is particularly valuable for operational ice centers.

2. Non-imaging radar

This type of sensor, also called a scatterometer, measures the amount of reflected energy, or backscatter, from the earth's surface. It cannot obtain the same detail as a SAR sensor, but it does provide complete, daily data about sea ice day and night, through cloud cover. Images from non-imaging radar have about the same level of detail as passive microwave imagery. The SeaWinds sensor aboard NASA's Quick Scatterometer (QuikSCAT) satellite provides daily, global views of ocean winds and sea ice.

2. Objective

1. To derive velocity of the Lambert glacier-Amery Ice shelf system using microwave and optical remote sensing data.
2. To analyse the temporal variation of glacier velocity in the Lambert glacier.
3. To study the effects of elevation, blue ice areas and melting dynamics on the derived glacier velocity.

3. Study Area

The largest glacier in the world is the Lambert-Fisher Glacier in Antarctica. At 400 kilometers (250 miles) long, and up to 100 kilometers (60 miles) wide, this ice stream alone drains about 8 percent of the Antarctic Ice Sheet. Antarctica, the ice continent, being a “Scientists Paradise” for biological, meteorological and geological research, serves as a living laboratory to measure the effects of prevailing climate change. As of date, there are 44 permanent bases of 18 countries including India in Antarctica where research in various fields is being conducted. Antarctic research has a global relevance in understanding broader physical and environmental changes as a storehouse of past records of local and global changes. The total volume of ice in the Antarctic Ice Sheet today is 27 million km, which is equivalent to 58 m of global sea level (i.e., if all the

ice in Antarctica melted, sea levels would rise by 58 meters). The Antarctic Ice Sheet is usually divided into three ice sheets: The Amery Ice Shelf (AIS) is the largest ice shelf in East Antarctica and buttresses the Lambert Glacier catchment basin, which accounts for 16% of the total mass of the East Antarctic Ice Sheet (Fricker *et al.* 2000). The AIS ice front is near 69°S, which is much further north than the ice fronts of the larger Ross and Filchner–Ronne ice shelves at, 78° S and, 74–78° S, respectively. The AIS is one of the largest ice shelves bordering the East Antarctic Ice Sheet. The Lambert, Mellor and Fisher Glaciers are the primary tributaries that flow into the AIS. The study area is 660 km wide and 380 km wide.

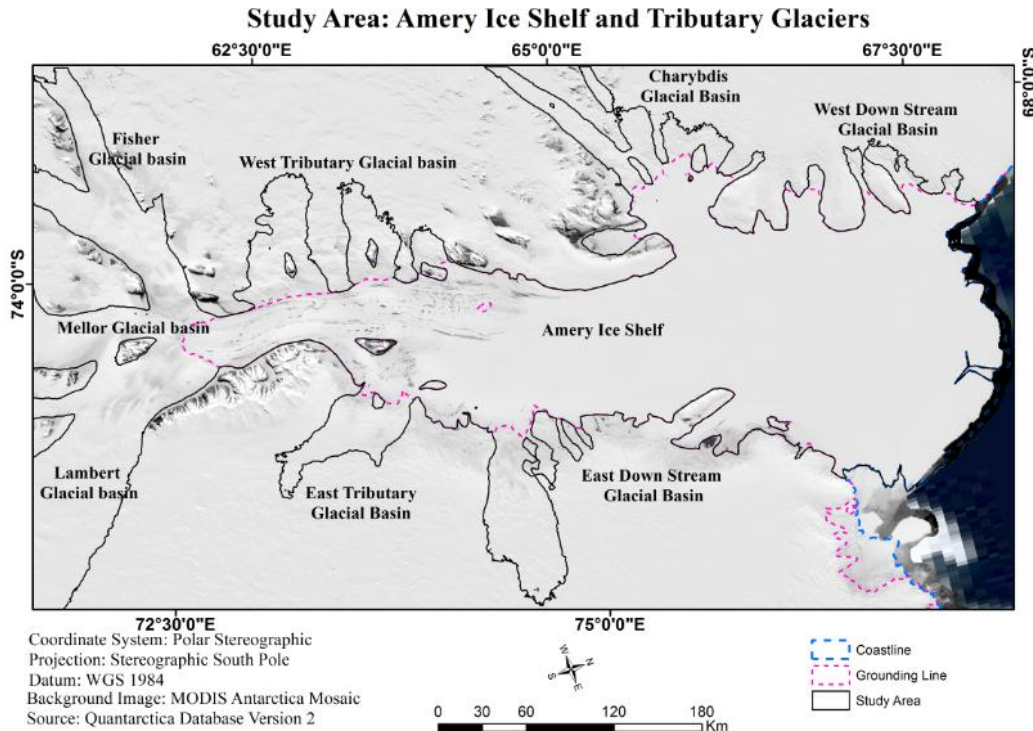


Figure 2: Study Area

4. Background

After the advent of SAR images most of the difficulties in the polar region have been resolved. The huge potential of SAR image processing has the power to map displacement in glaciers at centimeter resolution, hence becoming a powerful tool in glaciology. Glacier velocity is a phenomenon which helps to study about the climate change and also its implications on a larger extent. There are many ways to study the velocity of a glacier. Most of the studies are done using SAR and optical data. The methodologies which are used to study the velocity using SAR data include InSAR, DInSAR, offset tracking, and feature tracking which have given correct results. Feature tracking is one of the most effective ways to study glacier velocity using optical data.

4.1 SAR Interferometry

Retrieving surface velocities using both offset tracking and D-InSAR techniques and combining ascending and descending passes. To optimize the offset tracking technique, omit the azimuth offsets. By doing so, it improves the final resolution of the velocity product, as Sentinel-1 shows a lower resolution in the azimuth direction (Gómez, Navarro, 2017). Combine conventional Interferometric Synthetic Aperture Radar (InSAR) and Multiple Aperture InSAR (MAI) to determine the ice surface velocity (Gourmelen, Kim, Shepherd, 2011). Satellite synthetic aperture radar interferometric techniques make use of phase measurements as well as the more conventional amplitude measurements. Imaging radars are better adapted to conditions in the Polar Regions because they operate independent of cloud cover and solar illumination. In addition, when used interferometrically, imaging radars can yield precise information on the surface topography and ice velocity of entire area. In a Synthetic Aperture Radar (SAR) system, both the amplitude and the phase of the backscattered echoes are normally recorded. As the phase of a single SAR image is of no use however, conventionally only the amplitude or intensity image is usually provided to the end users. The phase difference of two backscattered SAR of the same ground surface area taken at slightly different view angles can however be utilized to generate digital elevation model (DEM) of the imaged terrain. This technique is known as SAR interferometry (InSAR) and can be extended to differential SAR interferometry (DInSAR) to detect small surface changes in the order of few centimeters.

The two SAR images are acquired from slightly different imaging geometries. Therefore, one SAR image must be precisely co-registered and resampled to the geometry of another SAR image. The former is called the slave image whereas the latter one is called the master image. The interferometric phase is then computed by multiplying each pixel of the first SLC with the complex conjugate of the corresponding pixel of the second co-registered SLC. Assuming no time delays in the imaging and/or any small atmospheric path delay, the estimated interferometric phase can be directly related to the difference in path length to a target from the satellite in the line of sight (LOS) direction and hence the surface topography can be estimated as per the geometry of the InSAR. The dual pass InSAR configuration is as shown in figure below. A point target O is located in the plane perpendicular to the flight direction. The distances from the two antennas to the point O are r_1 and r_2 , for A1 and A2, respectively. The two SAR antennae are separated by a baseline vector B, which can be decomposed into parallel and perpendicular components (B_{para} and B_{perp}) respectively. When two radar satellites, in different positions, image the same point on the ground, there is a difference in path length, ($\delta r = r_2 - r_1$) that is dependent on the Baseline separation of the two antennae (B). This gives a corresponding phase shift for the round trip.

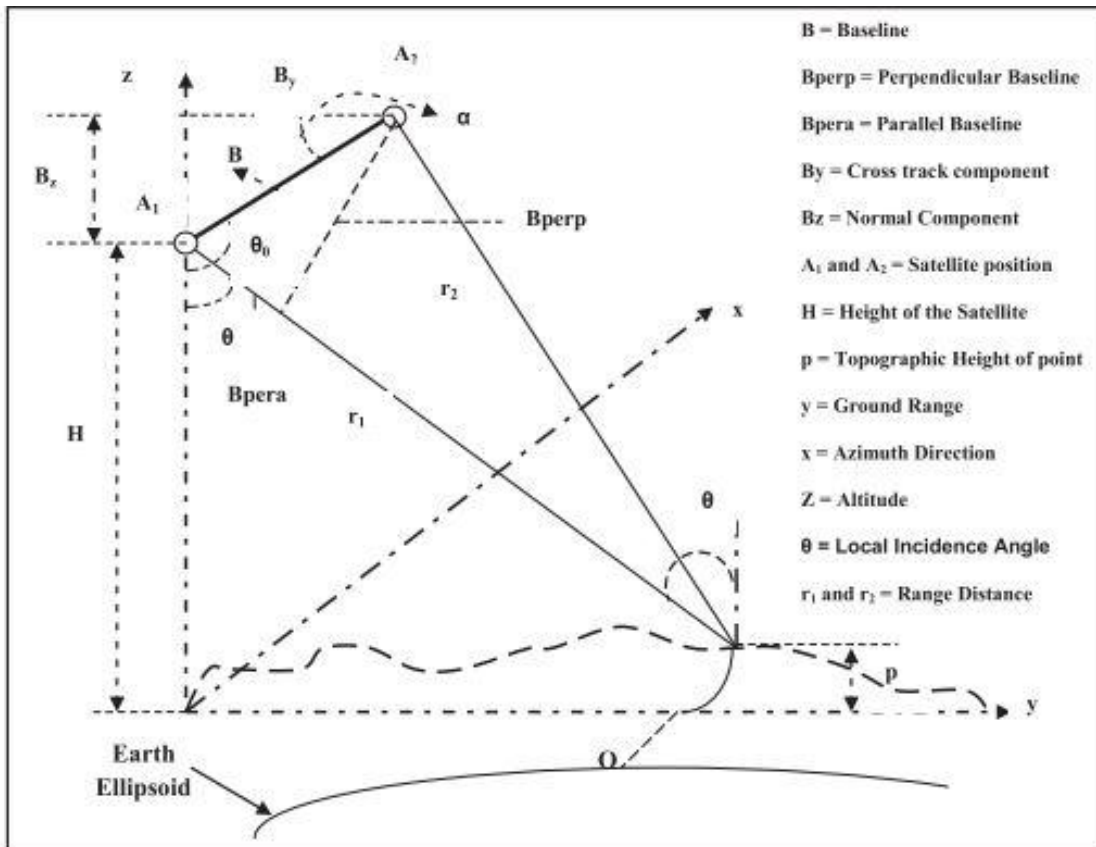


Figure 3: SAR Interferometry Principle

If the interferometric phase consists of a topographic and displacement term, the processing required to separate these two components goes under the name of differential interferometric processing. To identify the displacement component, the topographic phase has to be removed. This can be determined either from an external DEM from which interferometric fringes are simulated using the parameters of the interferometric system (perpendicular baseline length, slant range distance etc.) or from another interferometric pair, for which one assumes that other phase components are negligible. The difference of two interferograms can be used to measure small surface changes over large areas at a scale in the order of centimeters. The interferometric phase is sensitive to both surface topography and coherent displacement along the SAR look vector occurring between the acquisitions of the interferometric image pair. The basic idea in the differential technique is to remove the topography related phase while the remaining phase provides the displacement. In practice however, noise and path propagation related phases have to be taken into consideration. The phase φ measured by a repeat orbit InSAR system can be expressed as shown below.

$$\varphi = \frac{4\pi}{\lambda} \Delta r \quad (1)$$

Where Δr is the difference in range and includes components other than that contributed by the topography.

These components are summarized here

$$\varphi = \varphi_{terrain} + \varphi_{displacement} + \varphi_{atmosphere} + \varphi_{noise} + \varphi_{processing} \quad (2)$$

The phase due to noise comprises three components, thermal noise and baseline and temporal decorrelation. Other factors which must be taken into account are the phase due to processing errors, atmospheric displacement and the topographical phase. The phase due to processing errors is important but can also be considered as noise in the data. Similarly, the atmospheric displacement can be ignored in this case as the area of investigation is smaller than the spatial scale of the tropospheric variation. The most influential factor is the phase due to topography, which can either be estimated from a DEM or from another interferogram of a relatively large normal baseline component. The remaining phase after the removal of the unwanted phase components can be considered as a consequence of displacement and is expressed as in Equation 3 (Kenyi, 2003).

$$\varphi_{displacement} = \frac{4\pi}{\lambda} \rho \quad (3)$$

Radar interferometry has its limitations. If the glacier surface changes too significantly between successive imaging acquisitions, for instance due to surface melting, the distribution of scatterers at the surface of the glacier is altered, the fading pattern of the radar signal is modified and the phase coherence of the radar signal is no longer preserved, making it impossible to measure glacier velocities interferometrically. Similarly, phase coherence is destroyed when the glacier deformation across an image pixel exceeds half the radar wavelength, for instance due to excessive strain rates along shear margin.

The InSAR and DInSAR techniques have been used extensively to study glacier velocity across different regions which include mountain glacier as well as Arctic and Antarctic glaciers (Li, Benson, Gens, & Lingle, 2008 ; Taylor, 2016; Mattar et al., 1998; Ian Joughin, Rol Kwok, 1996; Ian Joughin, 2002; Hilmar et al., 2014; Kumar, Venkataramana, & Hogda, 2011).

4.2 Offset Tracking

Offset tracking means a technique that there is no need for phase unwrapping, one of the most critical steps in SAR interferometry.

First method to estimate the slant-range and azimuth registration offset fields of two SAR images is the intensity tracking, also known as cross-correlation optimization procedure. The offset fields are generated with a normalized cross correlation of image patches of detected real-valued SAR intensity images. The successful estimation of the local image offsets depends on the presence of nearly identical features in the two SAR images at the scale of the employed patches. When coherence is retained, the speckle pattern of the two images is correlated, and intensity tracking with small image patches can be performed to remarkable accuracy. Incoherent intensity tracking is also feasible but requires large image patches. In order to increase the estimation

accuracy, oversampling rates are applied to the image patches, and a two-dimensional (2-D) regression fit to model the correlation function around the peak is determined with a four-point interpolation. The location of the peak of the 2-D cross-correlation function yields the image offset. Confidence in the offset estimate is measured by comparing the height of the correlation peak relative to the average level of the correlation function to supply a correlation signal-to-noise ratio (SNR). Coarse information on the slant-range and azimuth offsets is used to guide the search of the cross-correlation maximum.

A method of measuring the offsets between SAR images complementary to the intensity tracking is the coherence tracking, also known as the fringe visibility algorithm or coherence optimization procedure. Throughout the single-look complex SAR images, small data patches are selected; a series of small interferograms with changing offset is constructed; and the coherence is estimated. The location of the coherence maximum is determined at sub-pixel accuracy by oversampling the single-look complex SAR image patches with zero-padding and by using a 2-D regression function to model the coherence peak with a four-point interpolator. The magnitude of the coherence maximum relative to the average level is used as a quality factor to help reject unsuitable patches. Coarse information on the slant-range and azimuth offsets is used to guide the search for the coherence maximum. For areas of insufficient coherence, such as observed for wet snow, no reliable offsets can be determined with this technique.

The image offsets in the slant-range and azimuth directions estimated with intensity and coherence tracking are related to the different satellite orbit configurations of the two SAR images and to the displacement occurring between the acquisition time intervals of the image pair. The estimation of glacier motion or surface deformation in general, requires therefore the separation of these two effects. The orbital offsets in the slant-range direction are related to the baseline, i.e., the separation in space of the antennas between the two SAR acquisitions. Orbital offsets in the azimuth direction are affected by the change of the baseline along the orbit. The estimation of the baseline from the orbit parameters supplied by the space agencies is normally not precise enough either for the determination of the orbital offsets or in general for SAR image coregistration. It is, therefore, preferable to determine the orbital offsets from stable reference points. After subtraction of the orbital offsets, pixel shifts in slant-range and azimuth directions are related to glacier motion only and are transformed to displacements in meters with knowledge of the SAR image pixel spacing (Strozzi, Luckman, Murray, Wegmüller, & Werner, 2002).

4.3 Optical Feature Tracking

Feature-tracking is a method that allows the estimation of a displacement between two images where first one is called reference image and a second image or search image. First, a window Ω_r is chosen in the reference image centered around pixel (i,j) . Then a window of same size is extracted from the search image but translated by (p,q) pixels within a specified search window Ω_s and compared to Ω_r using a function of similarity. This operation is repeated for different

values of (p,q) and the position of the maximum of similarity, interpolated to a fraction of pixel is a measure of the displacement (Dehecq et al., 2016).

The process of correlating two or more images containing the same image objects is called image matching. This method is used in several different fields besides deriving the velocity of glaciers. Examples of these are photogrammetric, image mosaicking, map updating, face detection, change detection, video coding, tectonics and monitoring of tumor growth. However, different fields often use different names for image matching based on the purpose of the matching. Image registration, motion estimation, particle tracking and optical flow are all words that are used and that essentially mean the same as image matching. When the purpose of image matching is to derive glacier velocities, it is important that the time span between the images is long enough to detect significant displacements, but short enough so that the objects are still recognizable. The length of this time span can vary with the velocities of the glaciers, the resolution of the images, the accuracy of the matching method, the amount of surface melt and the strain rates. The longer the time span is, the larger the displacement is compared to the accuracy of the match, but the chance of having too large surface transformation to get a correct match increases.

Until the 1980s, image matching was done by manually inspecting the images and identifying the same objects in the images from two different times. This work was very time consuming and there were no possibilities for obtaining sub-pixel measurements. Scambos et al., (1992) was the first to do image matching automatically on glaciers. They used image matching algorithms based on normalized cross-correlation (NCC) and the work of Bernstein (1983). They found that doing this automatically was not just less time consuming, but it was also more accurate than doing it manually. After this first demonstration, different image matching methods have been applied in glaciological studies. Image matching methods can be either area-based or feature-based. Area based methods operate directly on image quantities like brightness or phase. Feature-based methods on the other hand match features that are extracted from the images in a pre-processing step. Such features can be crevasses, stones or other differences in digital numbers (DN). The size of the windows to be correlated is important in glaciological studies. The window size has to be large enough to ensure that texture and not noise is matched. For small window sizes it is difficult to distinguish between texture and noise. But it is also important that the window size is small enough to avoid much deformation within the window. The optimal window size varies from glacier to glacier depending on glacier characteristics like visual contrast and the amount of deformation within the window. The optimal window size also depends on whether spatial or frequency domain methods are being used. Frequency domain methods generally require larger window sizes than spatial domain methods. This is because frequency domain methods are less accurate at small window sizes as a consequence of Heisenberg's uncertainty principle. The desired spatial resolution of the resulting image depends on the images to correlate. Commonly, studies aim at images with highest possible spatial resolution, but this is not the best choice in every situation. Higher spatial resolution images cover in general smaller areas. Therefore such images are less likely to cover stable ground that

can be used to coregister the images. This is particularly an issue for the large ice caps, ice sheets and ice shelves of the world.

There are many different correlation algorithms that have been used to derive velocities. It comprises of (1) normalized cross-correlation operated in the frequency domain, (2) cross correlation operated in the frequency domain, (3) phase correlation operated in the frequency domain, (4) cross-correlation operated in the frequency domain on orientation images, (5) phase correlation operated in the frequency domain on orientation images, (6) the phase correlation algorithm used in the COSI-Corr software. Cross-correlation on orientation images (CCF-O) outperforms the three similar Fourier methods, both in areas with high and low visual contrast. Normalized cross-correlation (NCC) experiences problems in areas with low visual contrast, areas with thin clouds or changing snow conditions between the images. CCF-O has problems on narrow glaciers where small window sizes are needed, and it obtains fewer correct matches than COSI-Corr in areas with low visual contrast. COSI-Corr has problems on narrow glaciers and it obtains fewer matches compared to CCF-O when thin clouds cover the surface or if one of the images contains snow dunes. Of the three methods NCC, CCF-O and COSI-Corr, only CCF-O manages to match striped Landsat images after the failure of the Scan Line Corrector (SLC on) in 2003. In conclusion, CCF-O and COSI-Corr are considered to be the two most robust matching methods for global-scale mapping and monitoring of glacier velocities. The MEDICIS correlator software, developed at CNES and commercially available has also been used to perform feature tracking using ASTER and SPOT images. Some other papers measured the velocities of six glacier tongues and a few tongues within ice shelves distributed around the Antarctic coastline by determining the displacement of crevasse patterns seen on sequential Landsat image.

COSI-Corr is a highly advanced matching program developed by Sébastien Leprince, 2007. It was originally made for investigating tectonics, but glaciologists soon found that it was also a valuable tool for deriving glacier velocities. It estimates the phase difference in the Fourier domain and does not transform the images back to the spatial domain to find the maximum of the CC. It is weighted by a bell-shaped window to centre the matching to the middle of the matching window. This makes it more certain where the match actually comes from within the window, but in cases with little contrast in the image centre it can still obtain matches in the outer part. The method obtains more correct matches than other tested methods in areas with little visual contrast and is also generally a very robust method. COSI-Corr is starting to become a commonly used program within glaciology. Many studies with respect to optical images available from different satellites have been used to study the glacier velocity using COSI-Corr. (Heid, 2011; Ruiz, Berthier, Masiokas, Pitte, & Villalba, 2015; Anderson, 2011; Scherler, Leprince, & Strecker, 2008).

Method	Number of Studies
Interferometric SAR	54
DInSAR	16
PSInSAR	4
SAR Tracking Techniques	47
Optical Feature Tracking	21
Image Matching	60
Aerial Photogrammetry	3

Figure 4: Methods used for Velocity Estimation

5. Data set

The dataset used here is Sentinel 1A and 1B.

Orbit: Sun-synchronous near polar orbit,

Band: C band, Wavelength: 5.55 cm,

Operational mode: Interferometric Wide Swath mode,

Temporal resolution: 6 days (1A and 1B combined),

Spatial Resolution: 5x20 m,

Swath: 240 km,

Polarization: Dual polarization (HH+HV, VV+VH).

Data Description

SAR data: Sentinel 1 A and 1 B

The SENTINEL-1 C-band radar antenna beam illuminates the ground to the right side of the satellite. Due to satellite motion and the along track (azimuth) beam width of the antenna, each target element only stays inside the illumination beam for a short time. As part of the on-ground processing, the complex echo signals received during this time are added coherently. In this way a long antenna is synthesized, with the synthetic aperture length being equal to the distance the satellite travelled during the integration time. In principle, the along track resolution obtainable with SAR is approximately half the real antenna length. To enhance the radiometric resolution, multi-look azimuth processing can be employed and consequently, the along track resolution will be reduced by a factor equal to the look number. The across track or range resolution is a function of the transmitted radar bandwidth. The fact that the system works coherently from end-to-end means that both the amplitude and the phase relationships between the complex transmitted and received signals are maintained throughout the instruments and the processing

chain. This facilitates aperture synthesis as well as multi-pass radar interferometry using pairs of images taken over the same area at different times.

The SENTINEL-1 Synthetic Aperture Radar (SAR) instrument may acquire data in four exclusive modes:

Stripmap (SM): This is a standard SAR stripmap imaging mode where the ground swath is illuminated with a continuous sequence of pulses and with the antenna beam pointing to a fixed azimuth and elevation angle.

Interferometric Wide swath (IW): Data is acquired in three swaths using the Terrain Observation with Progressive Scanning SAR (TOPSAR) imaging technique. In IW mode, bursts are synchronized from pass to pass to ensure alignment of interferometric pairs.

Extra Wide swath (EW): Data is acquired in five swaths using the TOPSAR imaging technique. EW mode provides very large swath coverage at the expense of spatial resolution.

Wave (WV). Data is acquired in small stripmap scenes called 'vignettes', situated at regular intervals of 100 km along track. The vignettes are acquired by alternating; acquiring one vignette at a near range incidence angle while the next vignette is acquired at a far range incidence angle.

Level-1 Ground Range Detected (GRD) products consist of focused SAR data that has been detected, multi-looked and projected to ground range using an Earth ellipsoid model. The ellipsoid projection of the GRD products is corrected using the terrain height specified in the product general annotation. The terrain height used varies in azimuth but is constant in range. Ground range coordinates are the slant range coordinates projected onto the ellipsoid of the Earth. Pixel values represent detected magnitude. Phase information is lost. The resulting product has approximately square spatial resolution and square pixel spacing with reduced speckle due to the multi-look processing. The noise vector annotation data set, within the product annotations, contains thermal noise vectors so that users can apply a thermal noise correction by subtracting the noise from the power detected image. The thermal noise correction is, for example, supported by the Sentinel-1 Toolbox (S1TBX). For the IW and EW GRD products, multi-look is performed on each burst individually. All bursts in all sub-swaths are then seamlessly merged to form a single, contiguous, ground range detected image per polarization channel.

The Interferometric Wide (IW) swath mode is the main acquisition mode over land for Sentinel-1. It acquires data with a 250 km swath at 5 m by 20 m spatial resolution (single look). IW mode captures three sub-swaths using Terrain Observation with Progressive Scans SAR (TOPSAR). With the TOPSAR technique, in addition to steering the beam in range as in ScanSAR, the beam is also electronically steered from backward to forward in the azimuth direction for each burst, avoiding scalloping and resulting in homogeneous image quality throughout the swath. TOPSAR mode replaces the conventional ScanSAR mode, achieving the same coverage and resolution as ScanSAR, but with a nearly uniform SNR (Signal-to-Noise Ratio) and DTAR (Distributed Target Ambiguity Ratio). IW SLC products contain one image per sub-swath and one per polarization channel, for a total of three (single polarization) or six (dual polarisation) images in an IW product. Each sub-swath image consists of a series of bursts, where each burst has been

processed as a separate SLC image. The individually focused complex burst images are included, in azimuth time order, into a single sub-swath image with black-fill demarcation in between, similar to ENVISAT ASAR Wide ScanSAR SLC products.

IW GRD High Resolution product characteristics per beam mode are:

Beam ID	IW1	IW2	IW3
Spatial Resolution rg x az m	20.4x22.5	20.3x22.6	20.5x22.6
Pixel spacing rg x az m	10x10	10x10	10x10
Incidence angle °	32.9	38.3	43.1
Equivalent Number of Looks (ENL)	4.4	4.3	4.3
Radiometric resolution	1.7	1.7	1.7
Range look bandwidth MHz	14.1	12.1	10.7
Azimuth look bandwidth Hz	315	301	301
Range Hamming weighting coefficient	0.70	0.73	0.75
Azimuth Hamming weighting coefficient	0.70	0.75	0.75

IW GRD High Resolution product characteristics common to all beams are:

Product ID	IW_GRD_HR
Pixel value	Magnitude detected
Coordinate system	Ground range
Bits per pixel	16
Polarisation options single	(HH or VV) or Dual (HH+HV or VV+VH)
Ground range coverage km	251.8
Absolute location accuracy m (NRT)	7
Number of looks (range x azimuth)	5 x 1
Look overlap (range x azimuth)	0.25 x 0.00

Figure 5: Sentinel 1A and B characteristics

Optical Data: Landsat 7 and 8

The government-owned Landsat 7 was successfully launched on April 15, 1999, from the Western Test Range of Vandenberg Air Force Base, California, on a Delta-II expendable launch vehicle. The Earth observing instrument on Landsat 7, the Enhanced Thematic Mapper Plus (ETM+), replicates the capabilities of the highly successful Thematic Mapper instruments on Landsats 4 and 5. The ETM+ also includes additional features that make it a more versatile and efficient instrument for global change studies, land cover monitoring and assessment, and large area mapping than its design forebears.

These features are:

- a panchromatic band with 15m spatial resolution
- on-board, full aperture, 5% absolute radiometric calibration
- a thermal IR channel with 60m spatial resolution
- an on-board data recorder

Landsat 7 is the most accurately calibrated Earth-observing satellite, i.e., its measurements are extremely accurate when compared to the same measurements made on the ground. Landsat 7's sensor has been called "the most stable, best characterized Earth observation instrument ever placed in orbit." Landsat 7's rigorous calibration standards have made it the validation choice for many coarse-resolution sensors. The excellent data quality, consistent global archiving scheme, and reduced pricing (\$600) of Landsat 7 led to a large increase of Landsat data users. In

October 2008, USGS made all Landsat 7 data free to the public (all Landsat data were made free in January 2009 leading to a 60-fold increase of data downloads). Considered a calibration-triumph, the Landsat 7 mission went flawlessly until May 2003 when a hardware component failure left wedge-shaped spaces of missing data on either side of Landsat 7's images. Six weeks after suffering the loss of its scan line corrector (SLC), the ETM+ resumed its global land survey mission resulting in only a short suspension of its imagery acquisitions for the U.S. archive. However, the malfunction has impacted the imagery of Landsat 7. Specifically, the ETM+ optics contain the Scan Mirror and Scan Line Corrector assembly among other components. The Scan Mirror provides the across-track motion for the imaging, while the forward velocity of the spacecraft provides the along-track motion. The Scan Line Corrector (SLC) assembly is used to remove the "zigzag" motion of the imaging field of view produced by the combination of the along- and across-track motion. Without an operating SLC, the ETM+ line of sight now traces a zigzag pattern across the satellite ground track. In this SLC-off mode, the ETM+ still acquires approximately 75 percent of the data for any given scene. The gaps in data form alternating wedges that increase in width from the center to the edge of a scene. The remainder of the ETM+ sensor, including the primary mirror, continues to operate, radiometrically and geometrically, at the same high-level of accuracy and precision as it did before the anomaly; therefore, image pixels are still accurately geolocated and calibrated. To fulfill the expectations of the user community for full coverage single scenes, data from multiple acquisitions are being merged to resolve the SLC-off data gaps. In all cases, a binary bit mask is provided so that the user can determine where the data for any given pixel originated. The USGS is continuing to research other methods of providing better merged data products, and will continue to provide information resulting from this work as it becomes available.

Landsat 8 carries two push-broom instruments: The Operational Land Imager (OLI) and the Thermal Infrared Sensor (TIRS). The spectral bands of the OLI sensor provides enhancement from prior Landsat instruments, with the addition of two additional spectral bands: a deep blue visible channel (band 1) specifically designed for water resources and coastal zone investigation, and a new shortwave infrared channel (band 9) for the detection of cirrus clouds. The TIRS instrument collects two spectral bands for the wavelength covered by a single band on the previous TM and ETM+ sensors. Descriptions of the band designations for all Landsat sensors, and information about the comparisons between Landsat 8 and previous bands are also available. These sensors both provide improved signal-to-noise (SNR) radiometric performance quantized over a 12-bit dynamic range. (This translates into 4096 potential grey levels in an image compared with only 256 grey levels in previous 8-bit instruments.) Improved signal to noise performance enable better characterization of land cover state and condition. Products are delivered as 16-bit images (scaled to 55,000 grey levels). A Quality Assessment band is also included with each Landsat 8 data product. This band allows users to apply per pixel filters to the Landsat 8 Operational Land Imager (OLI)-only and Landsat 8 OLI/Thermal Infrared Sensor (OLI/TIRS)-combined data products.

Landsat 8 launched on February 11, 2013, from Vandenberg Air Force Base, California, on an Atlas-V 401 rocket, with the extended payload fairing (EPF) from United Launch Alliance, LLC. The Landsat 8 satellite payload consists of two science instruments—the Operational Land Imager (OLI) and the Thermal Infrared Sensor (TIRS). These two sensors provide seasonal coverage of the global landmass at a spatial resolution of 30 meters (visible, NIR, SWIR); 100 meters (thermal); and 15 meters (panchromatic).

Landsat 8 was developed as collaboration between NASA and the U.S. Geological Survey (USGS). NASA led the design, construction, launch, and on-orbit calibration phases, during which time the satellite was called the Landsat Data Continuity Mission (LDCM). On May 30, 2013, USGS took over routine operations and the satellite became Landsat 8. USGS leads post-launch calibration activities, satellite operations, data product generation, and data archiving at the Earth Resources Observation and Science (EROS) center.

Landsat 8 instruments represent an evolutionary advance in technology. OLI improves on past Landsat sensors using a technical approach demonstrated by a sensor flown on NASA's experimental EO-1 satellite. OLI is a push-broom sensor with a four-mirror telescope and 12-bit quantization. OLI collects data for visible, near infrared, and short wave infrared spectral bands as well as a panchromatic band. It has a five-year design life. The graphic below compares the OLI spectral bands to Landsat 7's ETM+ bands. OLI provides two new spectral bands, one tailored especially for detecting cirrus clouds and the other for coastal zone observations.

The OLI collects data for two new bands, a coastal band (band 1) and a cirrus band (band 9), as well as the heritage Landsat multispectral bands. Additionally, the bandwidth has been refined for six of the heritage bands. The Thermal Instrument (TIRS) carries two additional thermal infrared bands. Note: atmospheric transmission values for this graphic were calculated using MODTRAN for a summertime mid-latitude hazy atmosphere (circa 5 km visibility). TIRS collects data for two more narrow spectral bands in the thermal region formerly covered by one wide spectral band on Landsat 4–7. The 100 m TIRS data will be registered to the OLI data to create radiometrically, geometrically, and terrain-corrected 12-bit data products.

Landsat 8 is required to return 400 scenes per day to the USGS data archive (150 more than Landsat 7 is required to capture). Landsat 8 has been regularly acquiring 550 scenes per day (and Landsat 7 is acquiring 438 scenes per day). This increases the probability of capturing cloud-free scenes for the global landmass. The Landsat 8 scene size is 185-km-cross-track-by-180-km-along-track. The nominal spacecraft altitude is 705 km. Cartographic accuracy of 12 m or better (including compensation for terrain effects) is required of Landsat 8 data products.

Landsat-7 ETM+ Bands (μm)			Landsat-8 OLI and TIRS Bands (μm)		
			30 m Coastal/Aerosol	0.435 - 0.451	Band 1
Band 1	30 m Blue	0.441 - 0.514	30 m Blue	0.452 - 0.512	Band 2
Band 2	30 m Green	0.519 - 0.601	30 m Green	0.533 - 0.590	Band 3
Band 3	30 m Red	0.631 - 0.692	30 m Red	0.636 - 0.673	Band 4
Band 4	30 m NIR	0.772 - 0.898	30 m NIR	0.851 - 0.879	Band 5
Band 5	30 m SWIR-1	1.547 - 1.749	30 m SWIR-1	1.566 - 1.651	Band 6
Band 6	60 m TIR	10.31 - 12.36	100 m TIR-1	10.60 - 11.19	Band 10
			100 m TIR-2	11.50 - 12.51	Band 11
Band 7	30 m SWIR-2	2.064 - 2.345	30 m SWIR-2	2.107 - 2.294	Band 7
Band 8	15 m Pan	0.515 - 0.896	15 m Pan	0.503 - 0.676	Band 8
			30 m Cirrus	1.363 - 1.384	Band 9

Figure 6: Landsat 7 and 8 characteristics

Radarsat Antarctic Mapping Project (RAMP) Digital Elevation Model (DEM):

The high-resolution Radarsat Antarctic Mapping Project (RAMP) digital elevation model (DEM) combines topographic data from a variety of sources to provide consistent coverage of all of Antarctica. Version 2 improves upon the original version by incorporating new topographic data, error corrections, extended coverage, and other modifications. The 1 km, 400 m, and 200 m DEM data are provided in ARC/INFO and binary grid formats, and the 1 km and 400 m DEMs are also available in ASCII format. Data access is unrestricted, but users should register to receive e-mail notification of product updates and changes in processing.

The RAMP DEM was developed by integrating a broad variety of available topographic source data in a GIS environment. By combining the comparative advantages of all available sources, the developers were able to fully exploit the most detailed and accurate topographic information in each data set. Error checking procedures included global statistical analysis, cross-validation methods, and creation of a synthetic stereo image for visualizing and detecting gross errors in the elevation data (Liu 1999). A new data integration technique allowed the developers to produce a DEM that is both seamless and geomorphologically consistent with ice-covered and ice-free terrain. The DEM captures details of geomorphology, ranging from small-scale mountain valleys to extensive ice sheet drainage basins.

6. Software's Used

1. Offset Tracking is usually performed using open source Sentinel toolbox SNAP.

2. COSI-Corr a module embedded in ENVI to perform feature tracking procedures on optical images.
3. Software which was extensively used for Landsat image corrections and other band math operations is ENVI.
4. Arc Map 10.4 for interpretation, map making, and analysis.
5. R Studio for Image and Statistical Analysis.

7. Methodology

1. BIA Extraction

Blue-ice areas (BIAs) cover ~1% of the East Antarctic ice sheet and are visual evidence of persistent ablation. In these regions, more snow is sublimated and/or eroded than is accumulated. A BIA is formed once the complete firn layer is removed. Feedback processes, which enhance blue-ice formation through the difference in surface characteristics of snow and ice, are examined using sensitivity simulations. Blue-ice areas (BIAs) are a rare feature in Antarctica (occupying between 0.8 and 1.6% of the continent; Winther et al., 2001) and are commonly, but not exclusively, associated with nunataks. These rock outcrops represent a barrier to the strong katabatic winds that flow constantly from the interior of the ice sheet, with the resulting turbulent air flow responsible for removing surface snow, leaving a bare ice face. BIAs have no net annual accumulation, and ablation occurs mainly through sublimation, which can be much higher than over adjacent snowfields (Bintanja and Reijmer 2001), and through wind erosion, resulting in a local negative surface mass balance. BIAs tend to be smooth, although they may be rippled, which facilitates their use for aircraft with conventional landing gear rather than aircraft with skis. Other BIAs are associated with steep slopes, glacial valleys, or the lower parts of glacial basins, where accelerated katabatic winds can effectively remove snow leaving a smooth ice surface. For more information on BIAs see Bintanja (1999). Under steady state conditions, ice flows converge horizontally in the vicinity of BIAs, with upward ice flows at the margins of nunataks balanced by ice mass losses mainly due to sublimation at the surface (Bintanja 1999). These ice flows transport englacial material to the surface, with unusually large volumes of surface deposits found along the margins of BIAs adjacent to many nunataks and mountain ranges. Thus BIAs are also of interest because they can be a concentrated source of meteorites that have fallen over a wider region over many millennia, been trapped and transported within the ice, and covered by snow, before being exhumed on the surface (Corti et al. 2003). As of 1999, more than 20,000 meteorites had been discovered in Antarctic BIAs (Bintanja 1999).

The USGS now provides data in the GeoTIFF with Metadata format. ENVI software can easily convert the optical band data to ToA reflectance values when you open the USGS file that ends with “_MTL.TXT”. ENVI will automatically open the Landsat image as multiple files with the 6 or 7 bands of optical data as one of several files. To create a reflectance data file using ENVI Classic, from the ENVI main menu bar select Basic Tools |Pre-processing |Calibration Utilities |Landsat Calibration. Select the optical data file (it has six or seven bands) and the ENVI

Landsat Calibration dialog should open with all of the calibration parameters filled in. Click on the Reflectance radio button and enter an output file name.

For ENVI Standard, select from the Toolbox | Radiometric Correction | Radiometric Calibration. Select the optical data file and the Radiometric Calibration dialog opens. Under Calibration Type choose Reflectance and save the new file. As a reminder, reflectance values range from 0.0 to 1.0 and are stored in floating point data format.

Radiance: This option is available if the image has gains and offsets for each band. ENVI reads these values from metadata from the sensors listed above. Radiance is computed using the following equation:

$$L_{\lambda} = Gain * Pixel\ value + Offset$$

ENVI expects gains and offsets to be in units of W/ (m² * sr * μm). If so, then radiance will be in units of W/ (m² * sr * μm).

Reflectance: Top-of-atmosphere reflectance (0 to 1.0). This option is available if the image has gains, offsets, solar irradiance, sun elevation, and acquisition time defined in the metadata. ENVI reads these values from metadata from the sensors listed above. Reflectance is computed using the following equation:

$$\rho_{\lambda} = \frac{\pi L_{\lambda} d^2}{ESUN_{\lambda} \sin \theta}$$

Where:

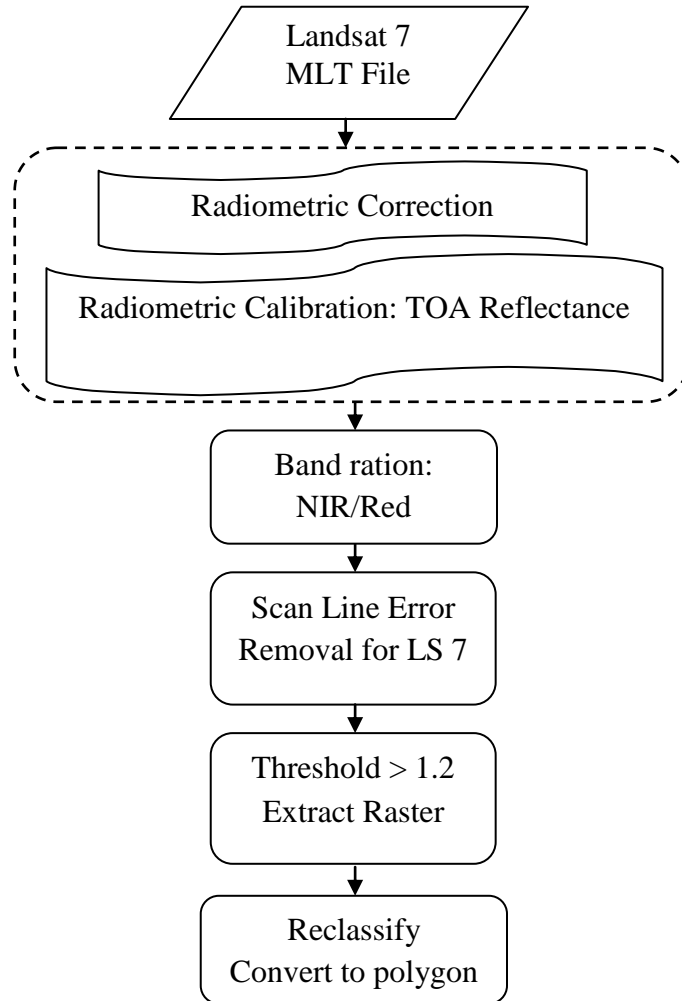
L_{λ} = Radiance in units of W/ (m² * sr * μm)

d = Earth-sun distance, in astronomical units.

$ESUN_{\lambda}$ = Solar irradiance in units of W/ (m² * μm)

θ = Sun elevation in degrees

The threshold which was selected for the extraction of Blue Ice Areas was nearly 1.1 to 1.3. The extracted raster values were converted to polygon after reclassification. The polygon was used to extract velocity. The statistics of the blue ice areas and the remaining areas was done using R Studio, statistical software.



2. Melt Duration Estimation:

The methodology followed to calculate Melt duration and Onset using Oscat, Scatsat, Ascet and Quicksat which are all scatterometers.

A. Backscatter time series analysis

The temperature was determined based on the backscatter threshold that indicates change in backscatter coefficient over some selected point in response to melting and freezing, for the analysis.

B. Mapping melting freezing over the ice-shelves

A threshold for each cell is applied which was determined from the above step the time series backscatter analysis. This is to map melting zones for each day. The number of days are added which are under the melt criteria.

C. Determination of melt onset and refreeze data

The melt onset day is determined with a condition of 3 day consecutive melt detection. The refreeze date is the start of a period of no melt for at least seven days.

D. Validation of results with Temperature data

Validation of melt condition and melt onset estimates can be performed by analyzing the corresponding brightness temperature measurements and AWS daily temperature data (Oza, 2015; Bothale et al., 2014).

3. Velocity Derivation (SAR Images)

Offset Tracking is a technique that measures feature motion between two images using patch intensity cross-correlation optimization. It is widely used in glacier motion estimation. Sentinel-1 Level-1 GRD Products Level-1 focused data are the generally available products intended for most data users. Level-1 products can be either Single Look Complex (SLC) or Ground Range Detected (GRD). Open the GRD products and apply orbit file for correcting the SAR datasets since the images appear inverted. Then Remove Border Noise for noise removal.

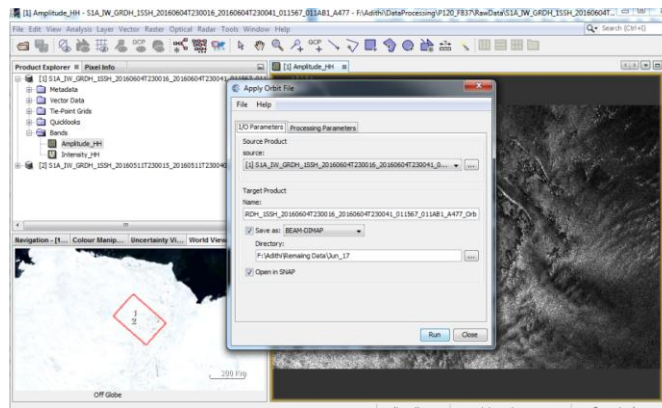


Figure 7: Apply Orbit File

For Offset Tracking processing, two images must be coregistered into a stack. The image that was acquired earlier is selected as the master and the other image is selected as the slave. The pixels in slave image will be moved to align with the master image with the help of the orbital data and a reference DEM. Coregistration ensures that each ground target from stationary scene contributes to the same (range, azimuth) pixel in both the master and the slave image.

For Offset Tracking application, DEM Assisted Coregistration should be used. It coregisters the products strictly based on the geometry using a DEM, orbit positions and times. This avoids possibly warping the image incorrectly due to the movement in the scene. Before image coregistration, the orbit state vectors in the original GRD product should be updated with the more accurate orbit data provided in the available orbit file.

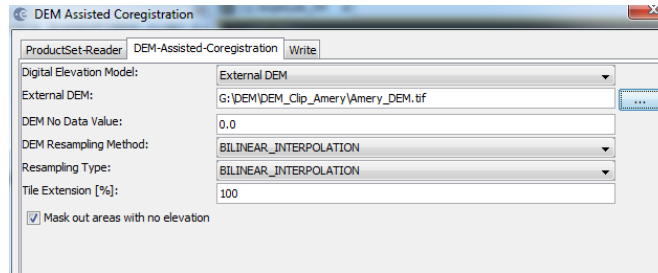


Figure 8: Dem Assisted Coregistration

The Offset Tracking operator estimates the movement of glacier surfaces between master and slave images in both slant-range and azimuth direction. It performs cross-correlation on selected Ground Control Point (GCP) in master and slave images. Then the glacier velocities on the selected GCPs are computed based on the offsets estimated by the cross-correlation. Finally the glacier velocity map is generated through interpolation of the velocities computed on the GCP grid. The Offset Tracking is performed in the following sub-steps in the algorithm:

1. For each point in the user specified GCP grid in master image, compute its corresponding pixel position in slave image using normalized cross-correlation.
2. If the compute offset between master and slave GCP positions exceeds the maximum offset (computed from user specified maximum velocity), then the GCP point is marked as outlier.
3. Perform local average for the offset on valid GCP points.
4. Fill holes caused by the outliers. The offset at hole point will be replaced by a new offset computed by local weighted average.
5. Compute the velocities for all points on GCP grid from their offsets.
6. Finally, compute velocities for all pixels in the master image from the velocities on GCP grid by interpolation.

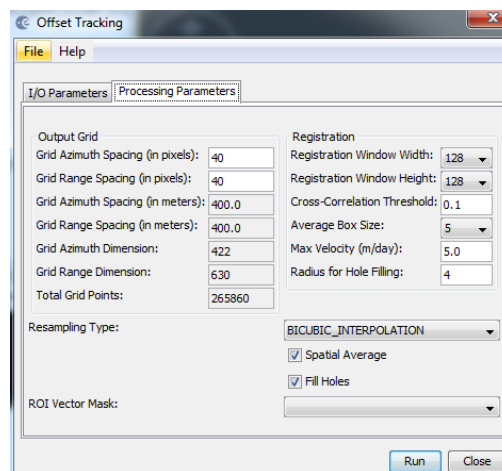


Figure 9: Offset tracking

The next and last step is geometric correction which is needed for correcting the image. A DEM is needed for terrain correction. The Velocity product is the output of this process which is delivered in m/day unit. The number of days in this process is 6 days to 36 days. The master and slave images must have a very low time difference.

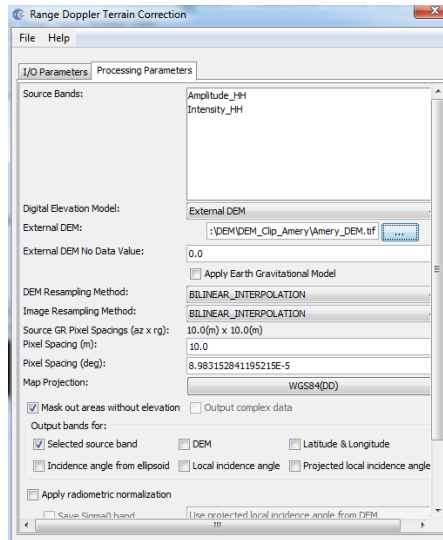
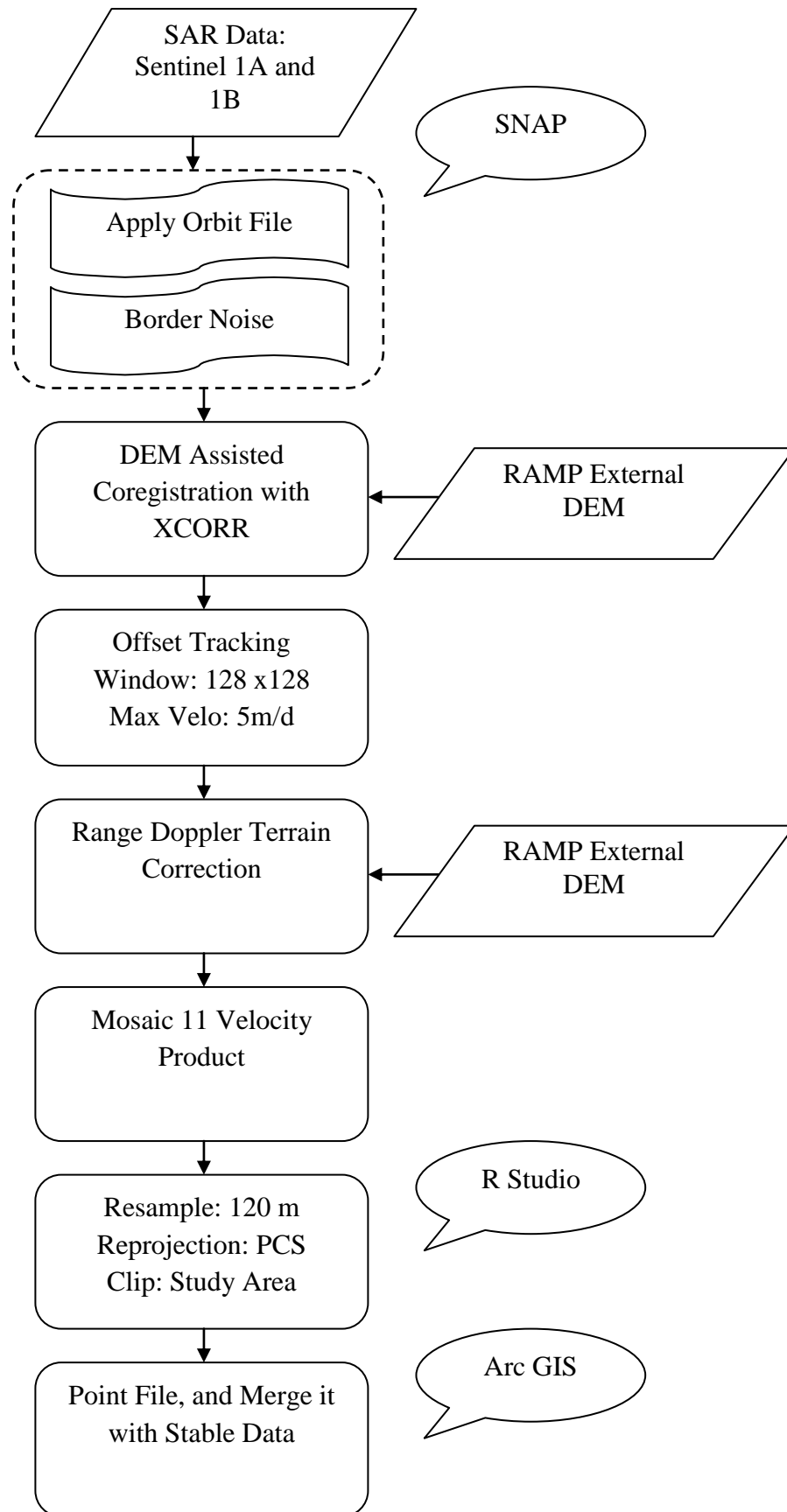


Figure 10: Terrain Correction



4. Velocity Derivation (Optical Images)

Feature tracking based on a cross-correlation algorithm that seeks offsets of the maximal correlation windows on repeated satellite images.

On 31 May 2003 the Landsat 7 Enhanced Thematic Mapper (ETM) sensor had a failure of the Scan Line Corrector (SLC). Since that time all Landsat ETM images have had wedge-shaped gaps on both sides of each scene, resulting in approximately 22% data loss. These images are available for free download from the USGS GloVis website and are found in the L7 SLC-off collection. In some cases you may want to perform pre-processing functions such as atmospheric correction or conversion of digital numbers to top-of-atmosphere reflectance on these images. Because these are scene-specific operations they cannot be applied correctly to a blended multi-date image. Any pre-processing functions such as these must be done before using this image gap-fill routine. Select Basic Tools | Preprocessing | Data-Specific Utilities | Landsat TM | Landsat Gapfill. This will open the Select input file(s) and processing type dialog. The one image triangulation method used in the Landsat Gapfill tool uses ENVI's DEM_BAD_DATA_DOIT to triangulate across image gaps.

Co- registration is the pixel by pixel matching and correlation is the degree of matching in image 1 and image 2. The cross-correlation is given by the equation:

$$CCC(u, v) = \frac{\sum_{x,y} (f(x, y) - \bar{f}) \times ((g(x + u, y + v) - \bar{g}(x + u, y + v)))}{\sqrt{\sum_{x,y} ((f(x,y) - \bar{f}))^2} \sqrt{\sum_{x,y} ((g(x+u,y+v) - \bar{g}(x+u,y+v)))^2}}$$

Here $f(x,y)$ and $g(x,y)$ are the pixel values in window Q and Q' of image 1 and image 2. u and v are the offsets between Q and Q' , \bar{f} and $\bar{g}(u,v)$ are the average pixel values of Q and Q' . The correlation window should be large enough to accommodate largest possible displacement.

The function (“Correlation”) correlates two images and provides a map of the relative displacements

Pre-event Image: Select the first image of the pair. This image is considered the reference or master. Post-event Image: Select the second image of the pair. The correlation result provides a displacement field using the convention eastward and northward positive. This displacement field is the horizontal ground displacement that should be added to the pre-event image to retrieve the post-event image.

Correlator engine: Select the correlator engine. Currently two correlators are available: frequential and statistical. The frequential correlator is Fourier based and is more accurate than the statistical one. It should be used in priority when correlating optical images. However this correlator is more sensitive to noise and is therefore recommended for optical images of good quality. The statistical correlator maximizes the absolute value of the correlation coefficient and is coarser but more robust than the frequential one. Its use is recommended for correlating noisy

optical images that provided bad results with the frequential correlator, or for correlating images of different content such as an optical image with a shaded DEM.

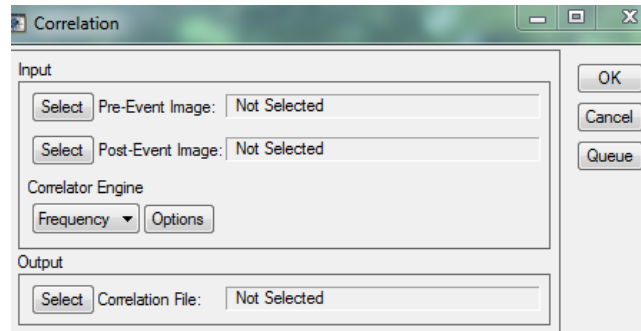


Figure 11: Correlation

Correlation File: Select the name of the correlation file to be created. If both images are georeferenced with the same projection and resolution, the georeferencing is accounted for, and only the geographic overlapping part is correlated. Otherwise, the correlation is pixel based. The parameters for the frequential correlator are:

Window Size: Size in pixels of the sliding window that will correlate the images. The size should be a power of two. The frequential correlator can be used in two modes:

- (a) The simple mode where a unique window size is specified. Leave the minimum window size field empty (“to (for multiscale)”).
- (b) The multi-scale mode. The multi-scale correlator accepts a maximum and a minimum window size. Patches with the largest window size are correlated first, and if the correlation succeeds, it is re-executed on patches with decreased size (power of two) and accounting for the displacement previously found. The process is iterated until the minimum window size is reached, or until the correlation fails. In this last case, the measurement found from the previous larger size is kept and the process moves on to the next patches. The multi-scale correlator is mostly useful under two situations:

When the displacements to estimate are greater than half the window size, in that situation, the correlator cannot determine the displacements. Use the multiscale correlator to set up a large window size which will be larger than two times the expected displacement, and a small size to the minimum acceptable window size in term of noise.

When the noise in the image is not uniformly distributed, using the multi-scale correlator will allow retrieving displacement in noisy areas (with large windows) and still use small windows in less noisy areas. It is customary to select the smallest window size that will provide a reasonable amount of noise as it will increase the density totally independent measurements.

Step: This parameter determines the step, in pixels, between two sliding windows. If the step is greater or equal to the window size, then all measurements will be independent.

Robustness Iteration: Number of times per measurement the frequency mask should be adaptively re-computed. The mask contributes in reducing the noise on the measurements. 2 to 4 iterations are satisfying in most cases Leprince et al. (2007).

Mask Threshold: Allows the masking of the frequencies according to the amplitude of the log-cross spectrum. A value close to unity is appropriate in most cases. See Leprince et al. (2007) for more details.

Resampling: Patches to correlate are relocated from sinc resampling. This option theoretically eliminates most of the biases at the sub-pixel scale. If used, the processing time is greatly increased (on average by a factor of 10). However, on noisy images, its usefulness has been noticed only on a very few occasions.

Grided Output: Check this option if you want to obtain a displacement map that can be superimposed with other displacements maps of the same area, or that can be mosaicked exactly. This tool (“Tools - Vector Field”) displays a vector field based on displacement maps or ASCII files. To load data in the Vector Field tool “File -- Open”.

“ENVI File”: When selected you will be prompted to enter the E/W band and N/S band successively of a displacement map to construct the vector field. The E/W and N/S band selected (and their subset) must be of the same size and must be georeferenced. A typical entry is a correlation file.

The centre coordinate window Q and correlated window Q' is (x,y) and (x+Δx, y + Δy) respectively. Then the displacement is calculated as follows:

$$D_h = \sqrt{(R_x \Delta x)^2 + (R_y \Delta y)^2}$$

where R_x and R_y are the pixel spacing in x and y directions.

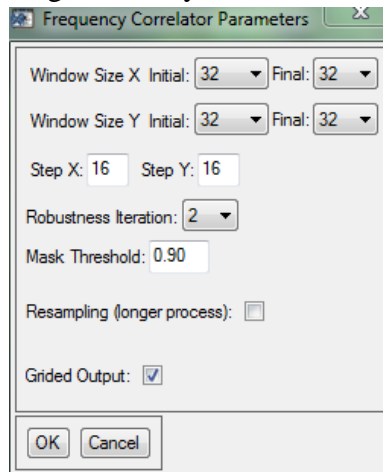
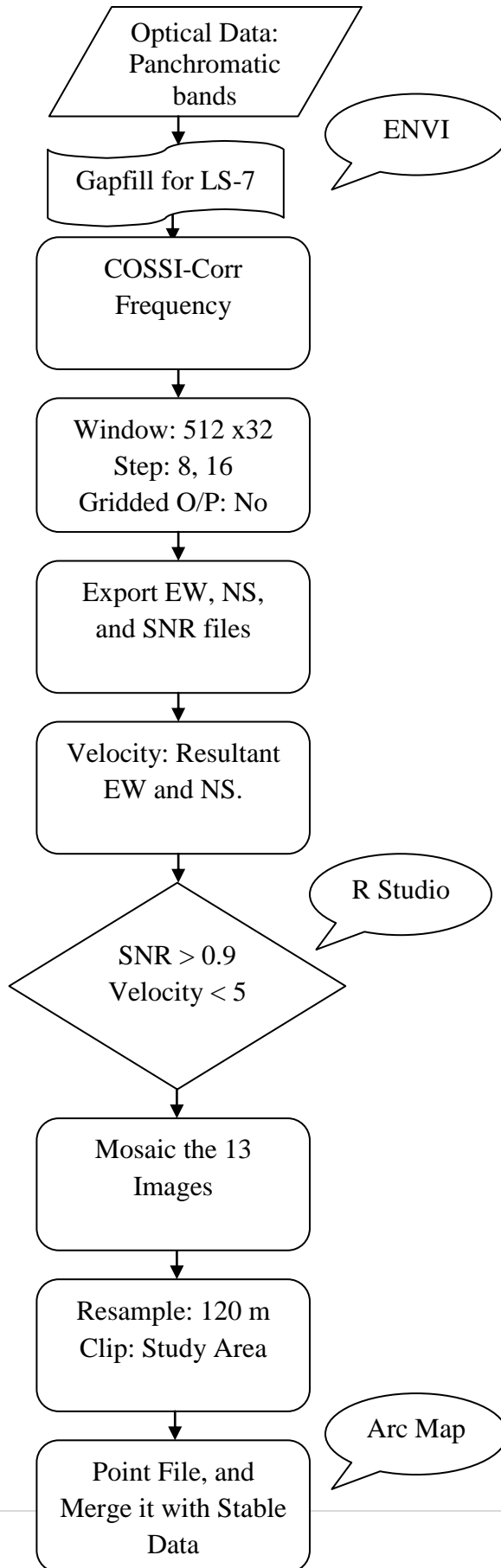


Figure 12: Frequency parameters

Save the output file in .img or .tif format and open it in ENVI. By using band math tool in ENVI calculate the resultant velocity. Thus, the result generated is resultant velocity of E-W and N-S direction. This process is repeated for all the paths and frames. Then using Arc Map the noise values are removed from resultant velocity file using the SNR. The condition adopted here is that SNR should be greater than 0.9. Then the velocity was filtered for the values less than 5 m per day. 5 m per day is the maximum velocity attained in this region.



8. Stable Dataset Generation

Once all the maps were derived a stable dataset was generated using the derived images and the available products from NSIDC and GoLIVE to generate a dataset which will be a stable dataset over any time period. This is by using the merge tool in Arc Map. The resultant velocity products were converted to point file and then merged. The merged shapefile is then interpolated using Ordinary Kriging and operator: mean for redundant points. The output is resampled to 120m.

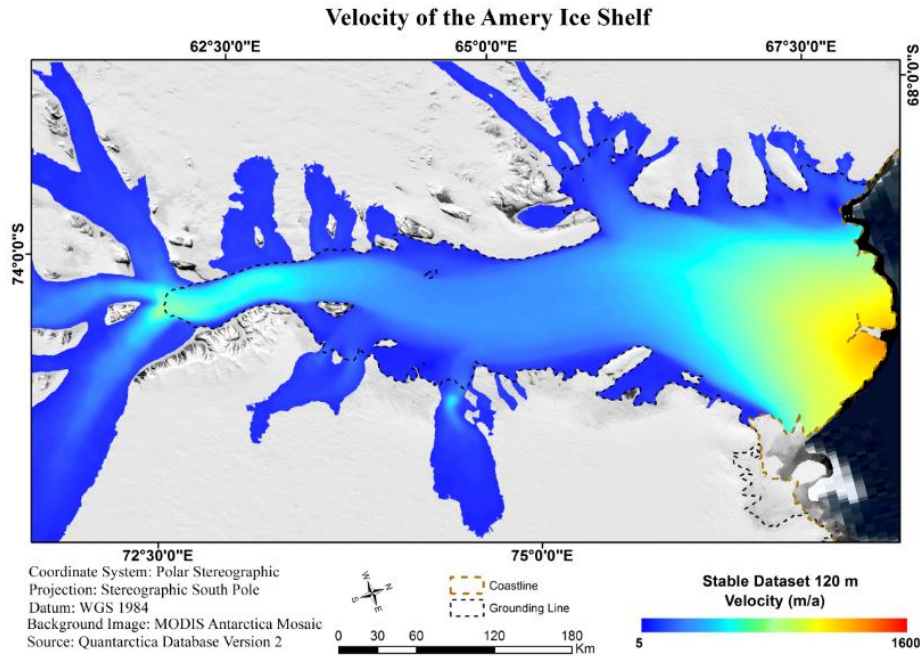


Figure 13: Stable Dataset generated

MEaSURES 450 m Ice Flow Velocity Data

National Snow and Ice Data Centre also provides a stable data set of glacier velocity which is derived using many techniques and also many other satellite data. The map is available for free at 450 m resolution. The velocity range is similar to the one derived by us.

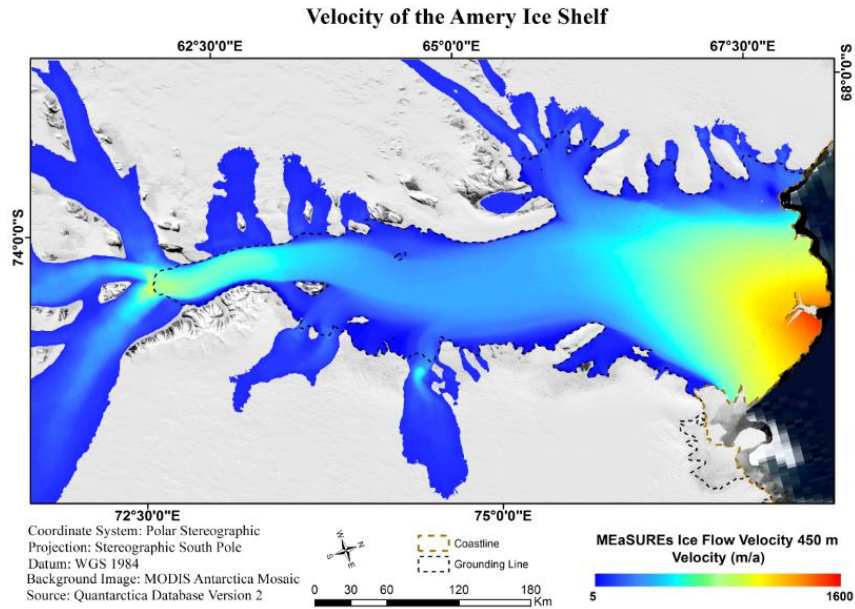
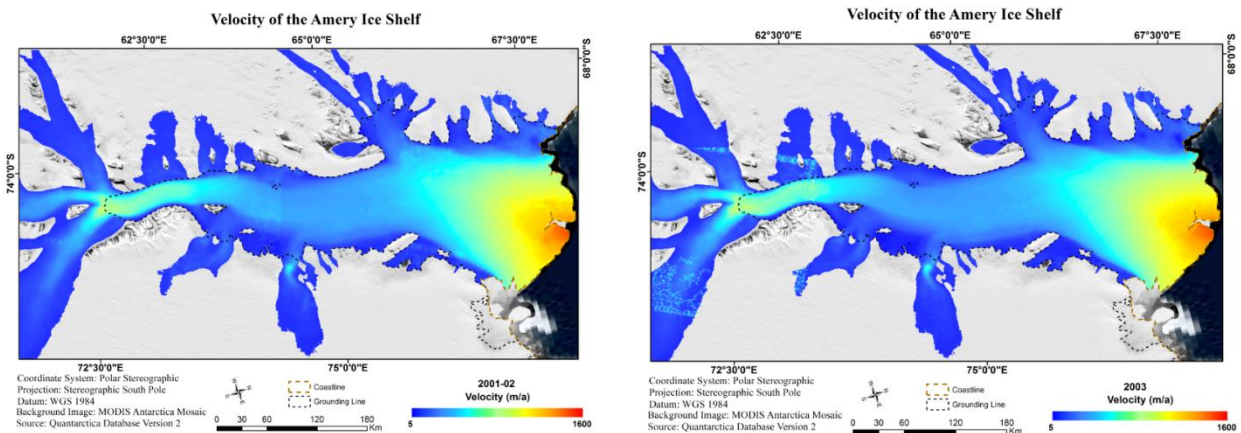


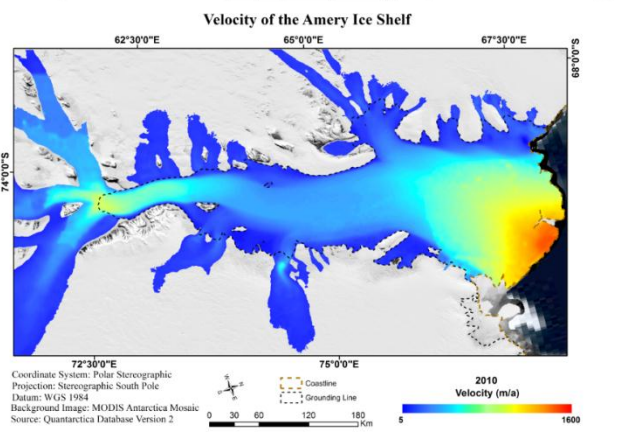
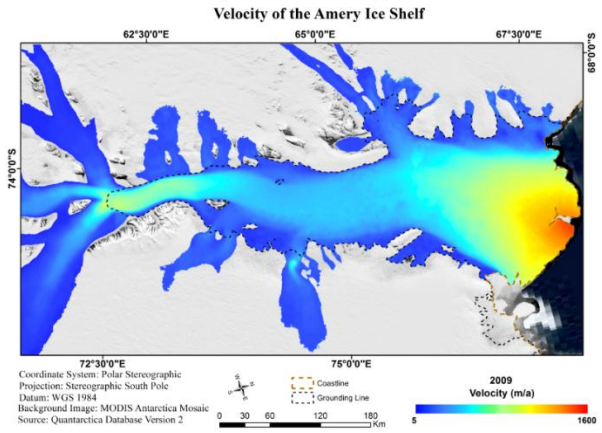
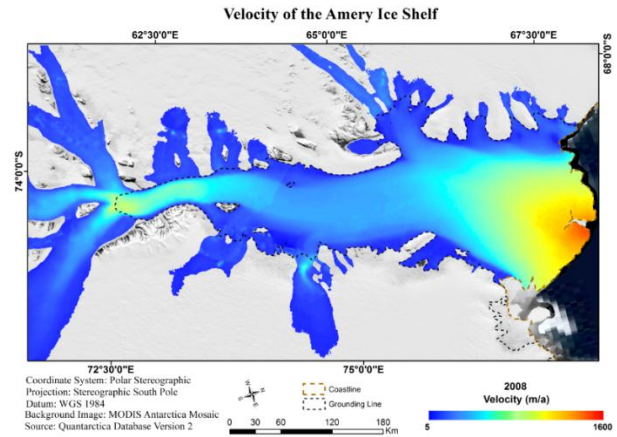
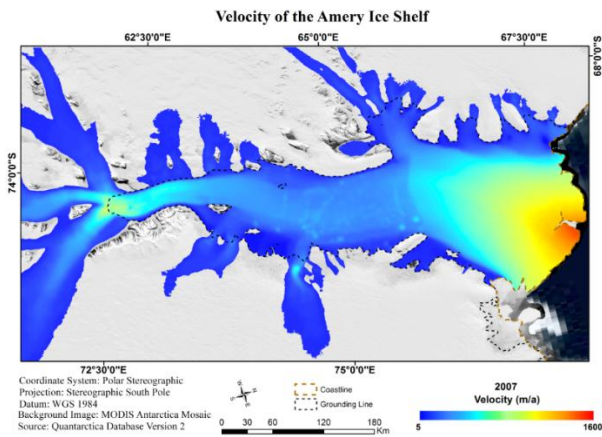
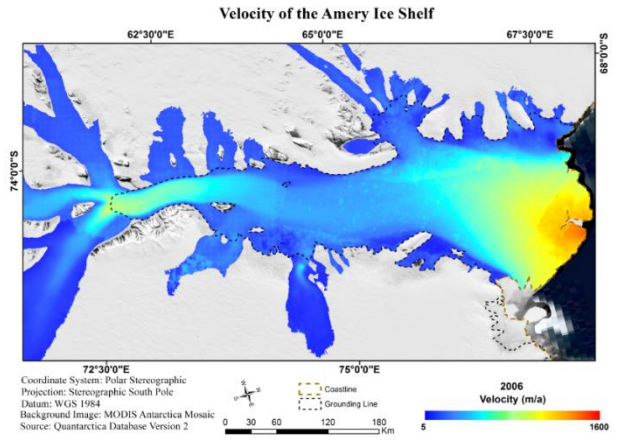
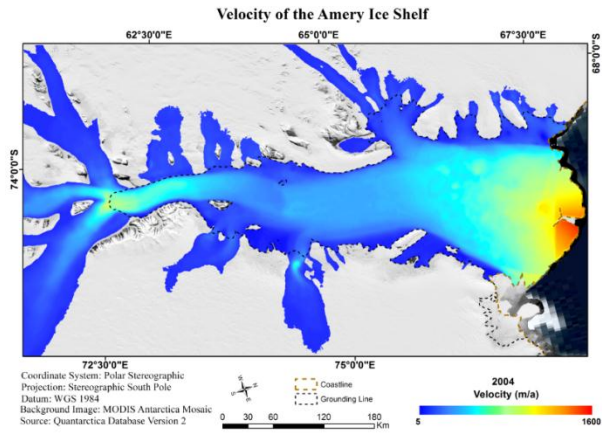
Figure 14: MEaSURES 450m

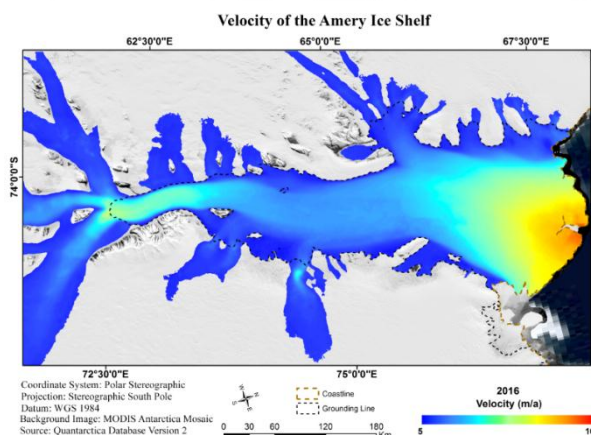
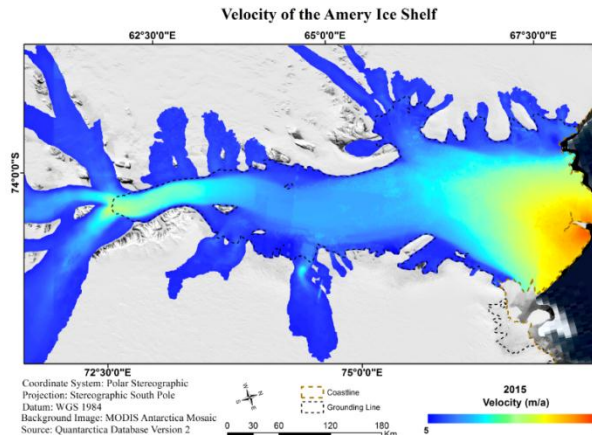
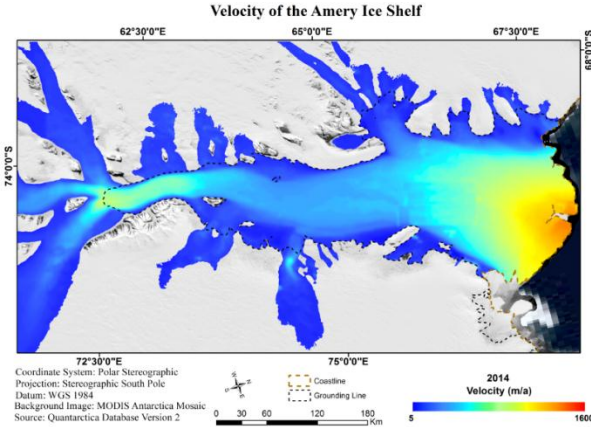
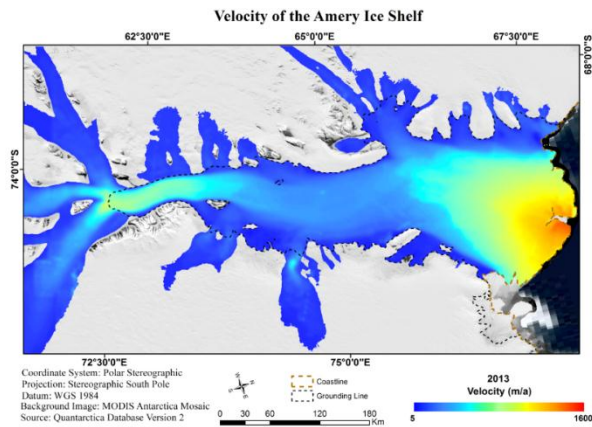
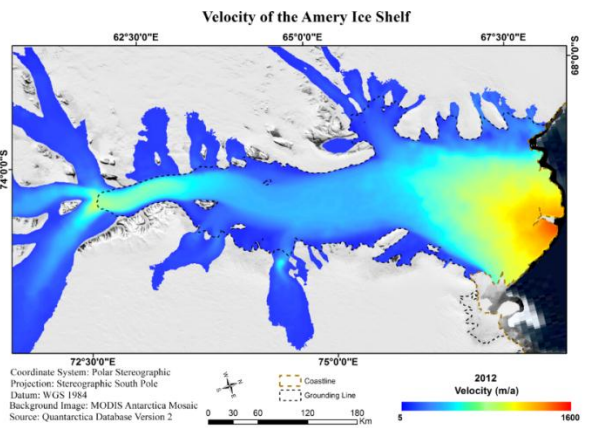
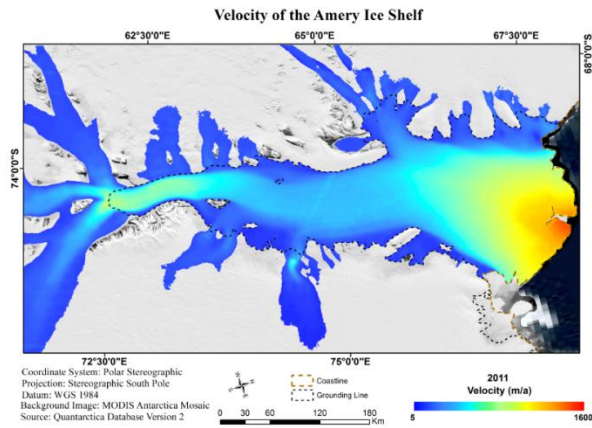
9. Results

9.1. Velocity

The optical images generated using Landsat 7 and 8 with COSI-Corr. The images were generated from 2001 to 2017 with almost 13 path frames. The path frames for Landsat images were acquired for the path 125 frames: 109-112; path 128 frames: 109-112; while path 130 frames: 108-112. The images were mosaicked and resampled to 120m. The velocity ranges from 5 to 1600 m per annum. The regions which were having No Data were merged with master or Stable Data.







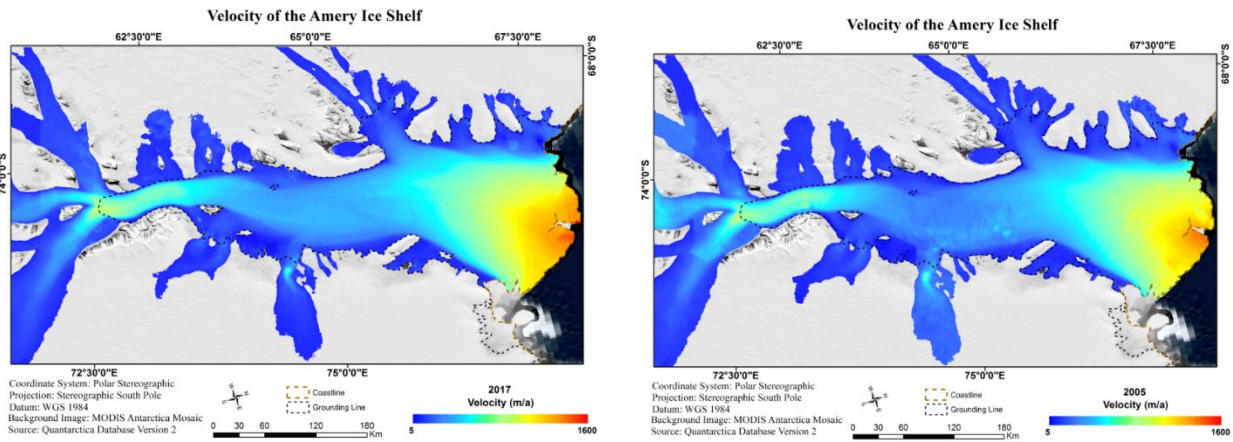


Figure 15: Yearly velocity maps generated

The Sentinel images are available from June 2016 till date. The velocity maps generated from August 2016 to March 2018. The total number of velocity maps generated was 19 using the open source SNAP. These maps are produced using the Offset tracking method. The number of path frames for the study region is 11. The common path 120 frame were 4 since the SAR images were unavailable in this region. The remaining 7 path frames available for the algorithm. Then the images were mosaicked. The resultant images were at 10 m, which were then resampled to 120m.

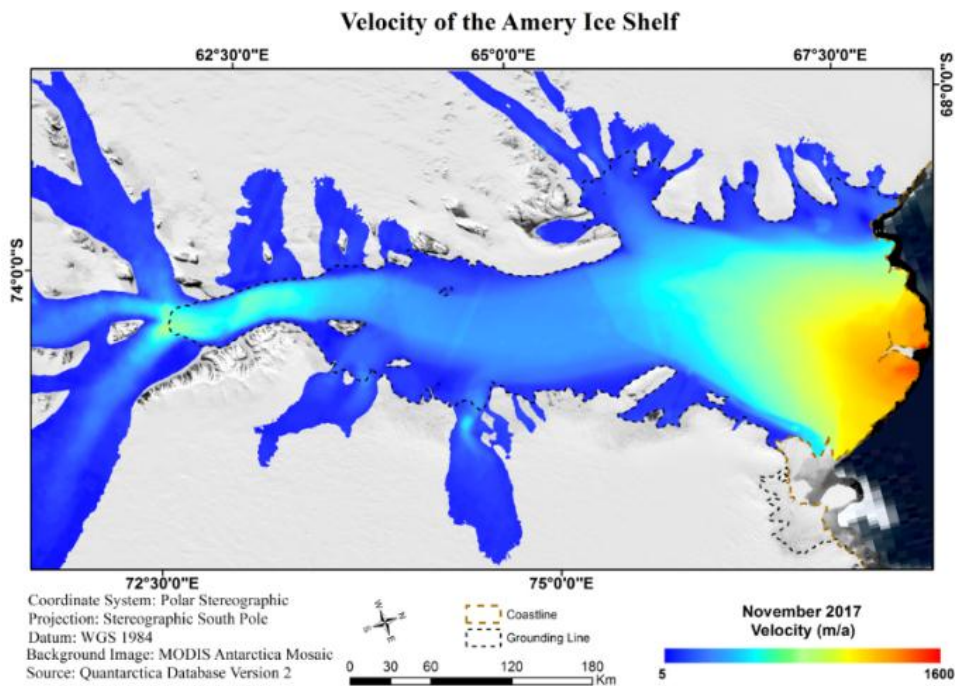


Figure 16: Monthly velocity maps generated

9.2. Blue Ice Areas

The effect of Blue ice areas was very clear in this study. The time period for this study was also from 2001 to 2017. The mean velocity extracted in the blue ice areas was lower than the overall mean velocity and also the non BIA areas. The highest velocity was in the non BIA areas. The bias, RMSE, Correlation map were produced for the yearly velocity variations in Blue Ice Areas for the time period of 17 years with respect to the MEaSURES Yearly, MEaSURES 450m, and Stable dataset generated.

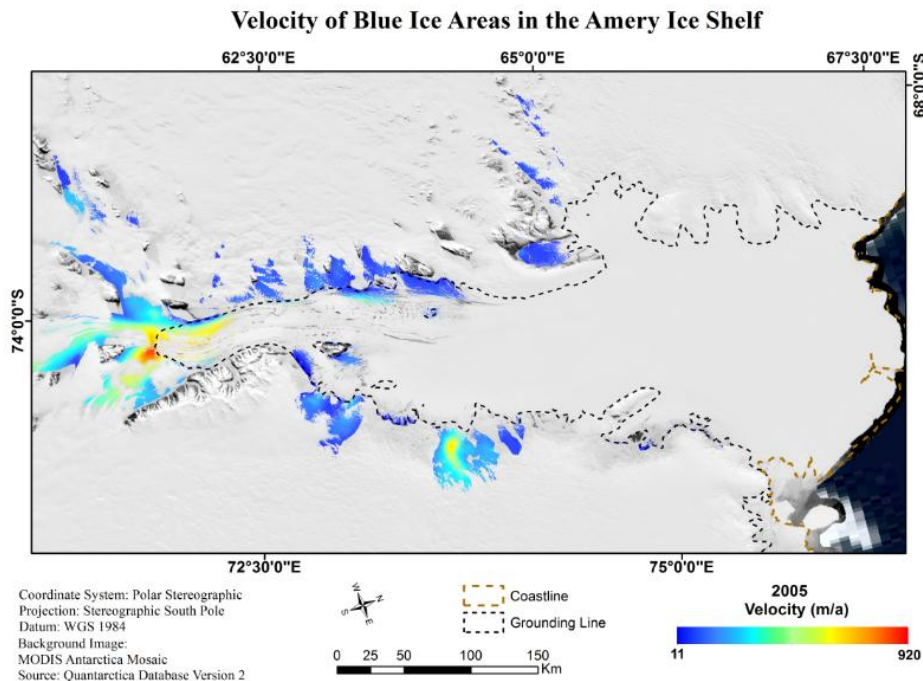


Figure 17: Blue Ice Area velocity

9.3. Melt

Melt distribution in the region was calculated using the scatterometer data for the time period 2001 to 2017. The velocity in high melt areas seems to be more than in the areas of low velocity. One of the consequences of global warming is the increase of melt on glaciers. This increase of melt could cause the glacier to move faster in the ablation zone and the glacier could decrease faster in size. The data shows that the melt only has a short term impact on the velocity. Annual average velocities do not seem to be much influenced by the melt, shown in these observations. The bias, RMSE, Correlation map were produced for the yearly velocity variations in different melt regions for the time period of 17 years with respect to the MEaSURES Yearly, MEaSURES 450m, and Stable dataset generated.

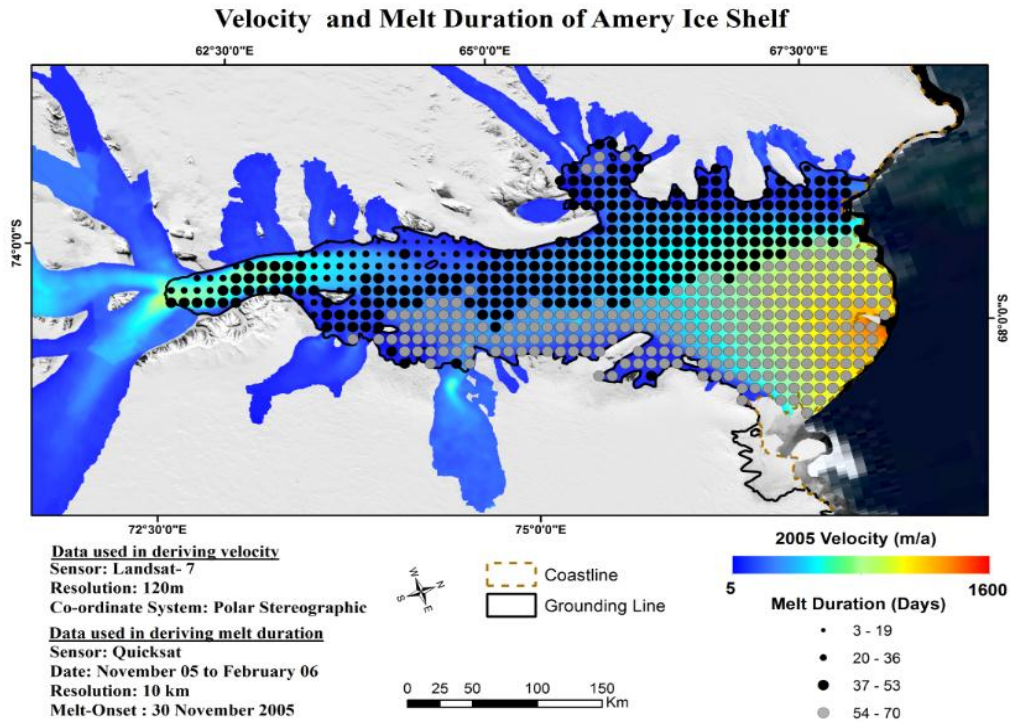


Figure 18: Melt Duration

9.4. Elevation

The velocity behaves in a peculiar way when it comes to elevated areas in the ice shelf. The highest velocity is in the lower elevation regions while the least is in the high elevated areas. The bias, RMSE, Correlation map were produced for the yearly velocity variations in Blue Ice Areas for the time period of 17 years with respect to the MEaSURES Yearly, MEaSURES 450m, and Stable dataset generated.

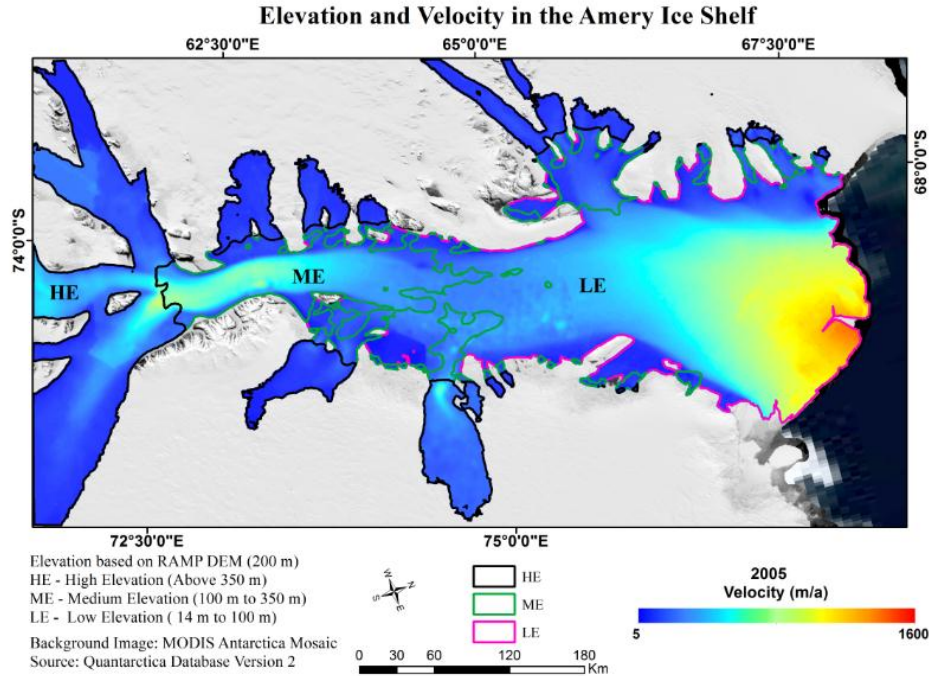


Figure 20: Elevation Distribution

10. Analysis

10.1. Slope

The error in the velocity map can be identified using the derivative of the velocity which is the slope. The slope was derived using R Studio. The slope maps generated are as shown below. It ranges from 0 to 10 degree. The value of slope also signifies strain in the region due to velocity.

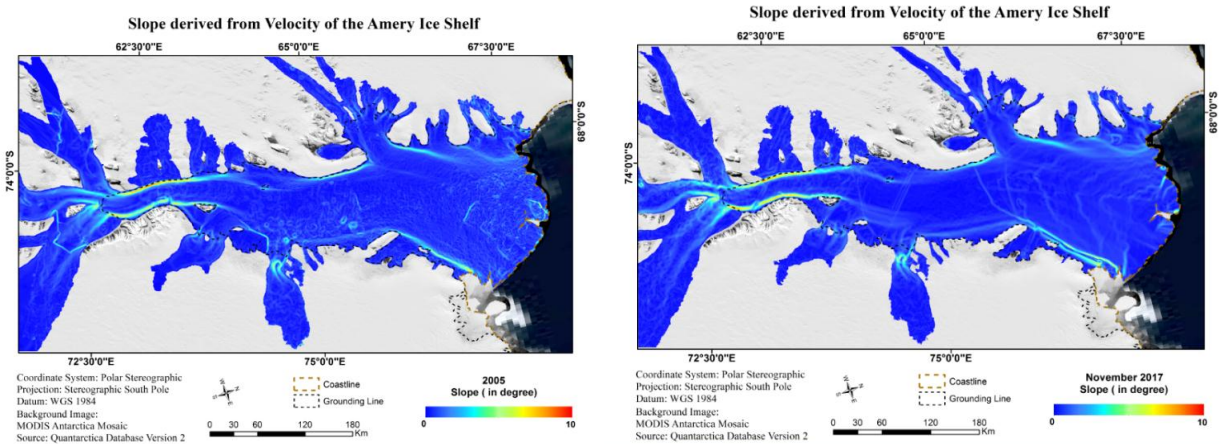


Figure 21: Slope Derived From Velocity

10.2. Velocity Analysis

Bias

The bias is calculated by using the published data from NSIDC which is at 450 m, yearly data and GoLIVE. The anomaly is calculated using these stable data. The range is from -200 to 300 m/a. This map is generated using R Studio.

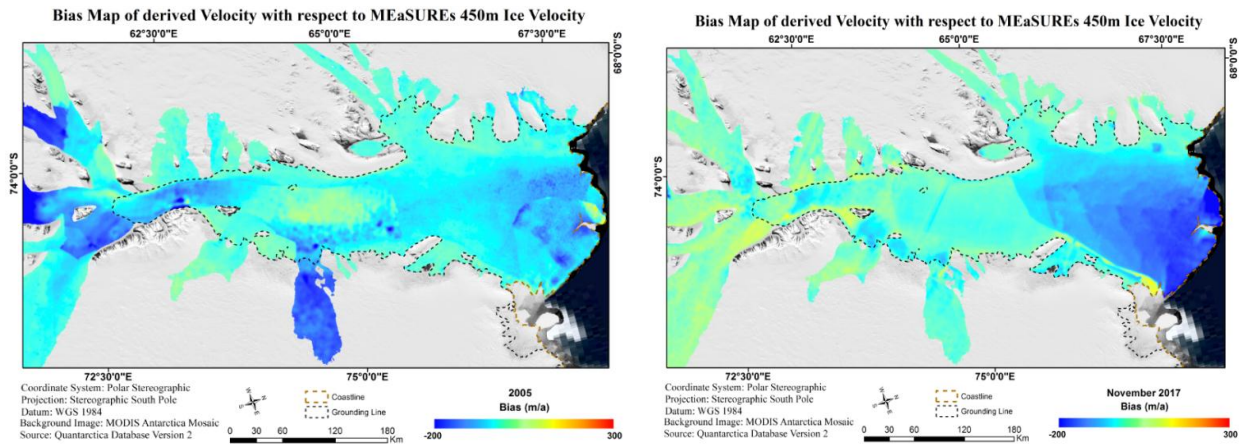


Figure 22: Bias with respect to MEaSUREs 450 m

RMSE

The RMSE is calculated by using the bias data calculated. The bias image is squared. The bias square image is then taken; an aggregate function is calculated over the local window (2 by 2). Then the cell value is replaced by the aggregate's square root value. The resolution of the resultant map is dependent on the window size. RMSE signifies the change rather than the error involved. This ranges from 0 to 300 m/a. This map is also generated using software called R Studio.

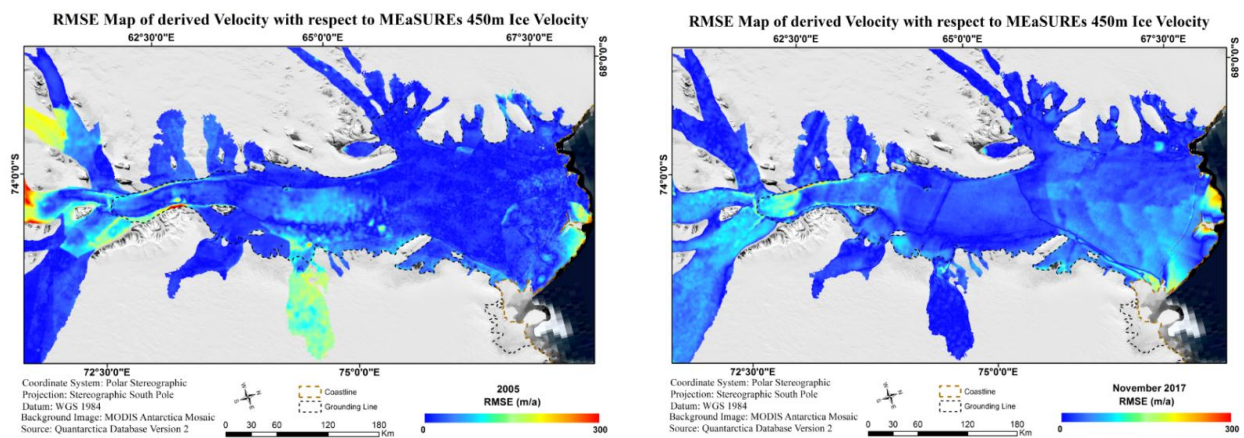


Figure 23: RMSE with respect to MEaSUREs 450 m

Correlation

The generated velocity maps were correlated with respect to Stable Dataset generated, MEaSUREs Ice Velocity at 450m, MEaSUREs Yearly and GoLIVE data. The Pearson's

correlation coefficient for a local window of 5 by 5 then the raster value was replaced by the coefficient and exported as a map. The range is from -1 to 1. This map is generated using R Studio. As per the map the velocity estimated seems to be quite accurate for both the SAR images and optical data.

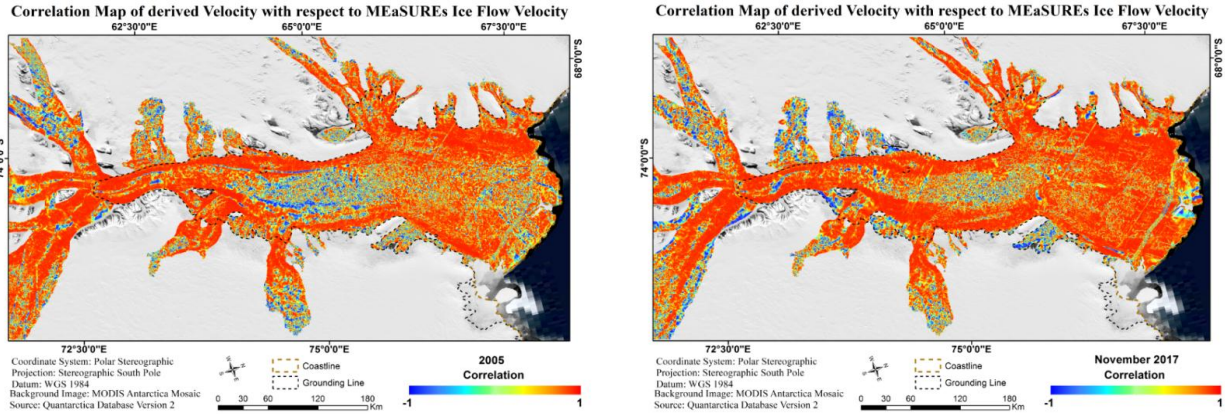


Figure 24: Correlation with respect to MEaSURES 450 m

10.3. BIA Analysis

Bias

The bias is calculated by using the published data from NSIDC which is at 450 m, yearly data and Stable dataset. The anomaly is calculated using these stable data. The range is from -150 to 200 m/a. This map is generated using R Studio.

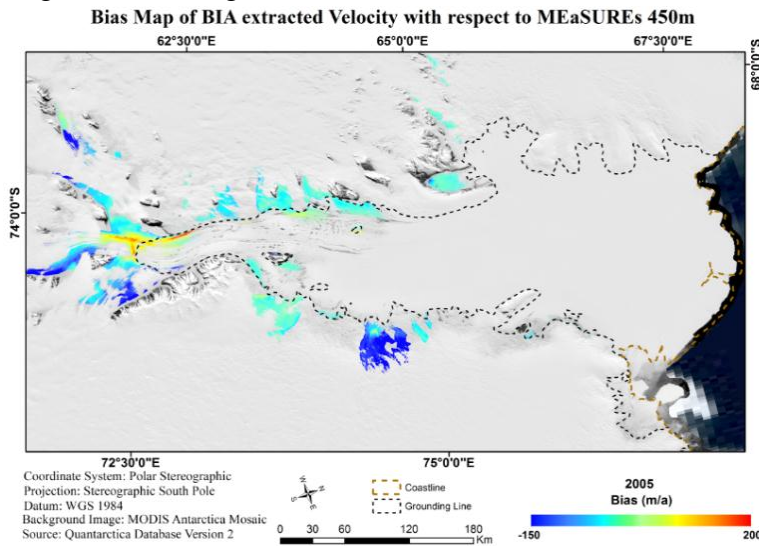


Figure 25: Bias of BIA's with respect to MEaSURES 450 m

RMSE

The values range from 0 to 200 m/a. This map is also generated using software called R Studio.

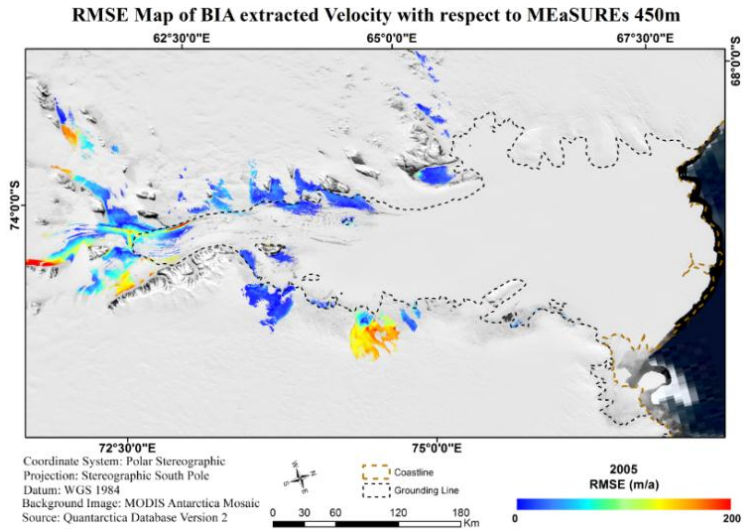


Figure 26: RMSE of BIA's with respect to MEaSUREs 450 m

Correlation

The generated velocity maps were correlated with respect to Stable Dataset generated, MEaSUREs Ice Velocity at 450m, MEaSUREs Yearly and GoLIVE data. The range is from -1 to 1. This map is generated using R Studio.

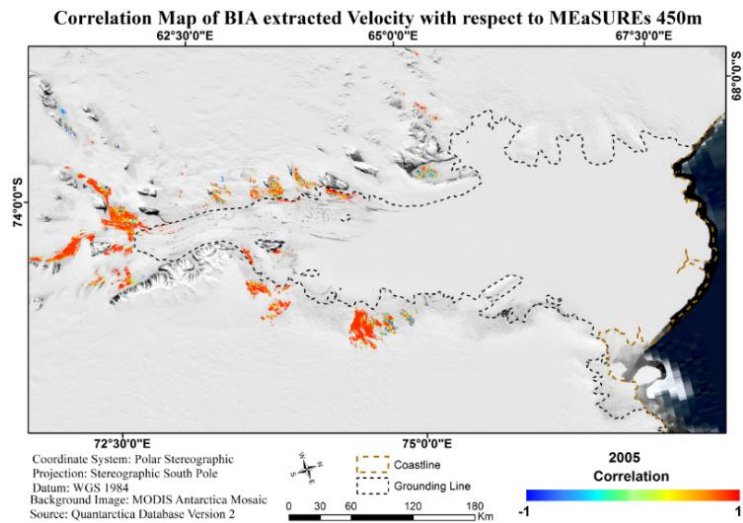


Figure 27: Correlation of BIA's with respect to MEaSUREs 450 m

10.4. Elevation Analysis

Bias

The bias is calculated by using the published data from NSIDC which is at 450 m, yearly data and Stable dataset. The anomaly is calculated using these stable data. The range is from -150 to 150 m/a. This map is generated using R Studio.

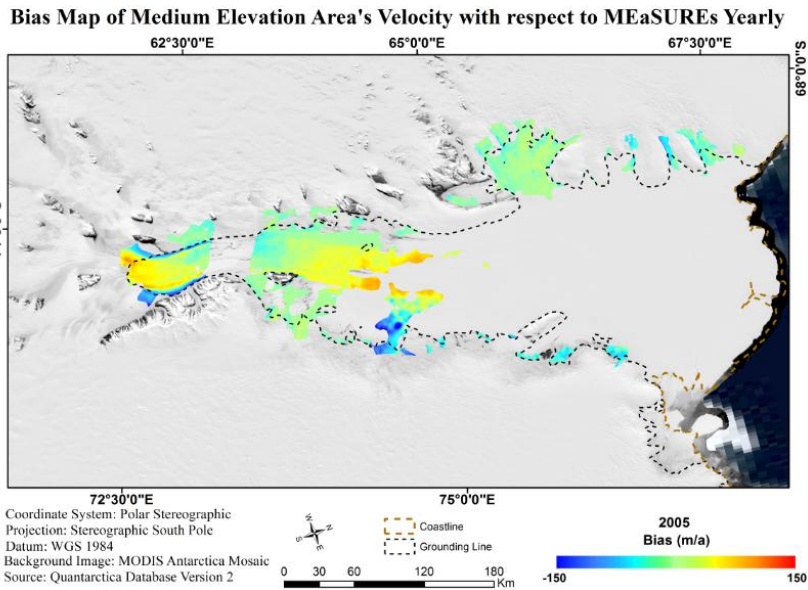
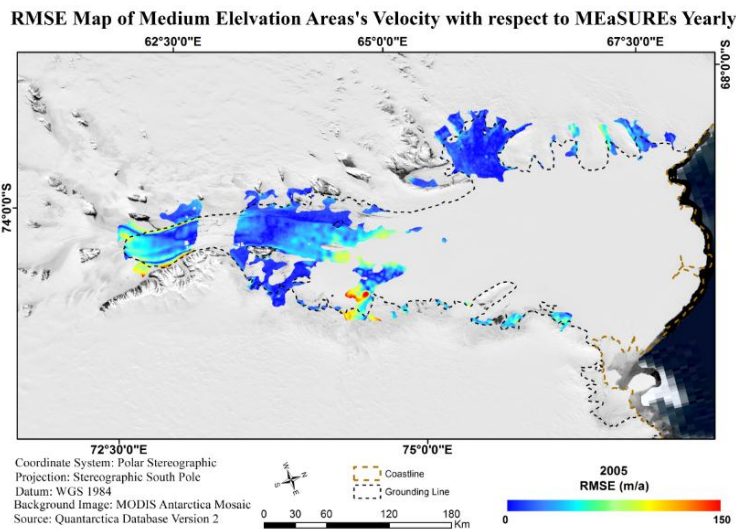


Figure 28: Bias of BIA's with respect to MEaSURES 450 m

RMSE

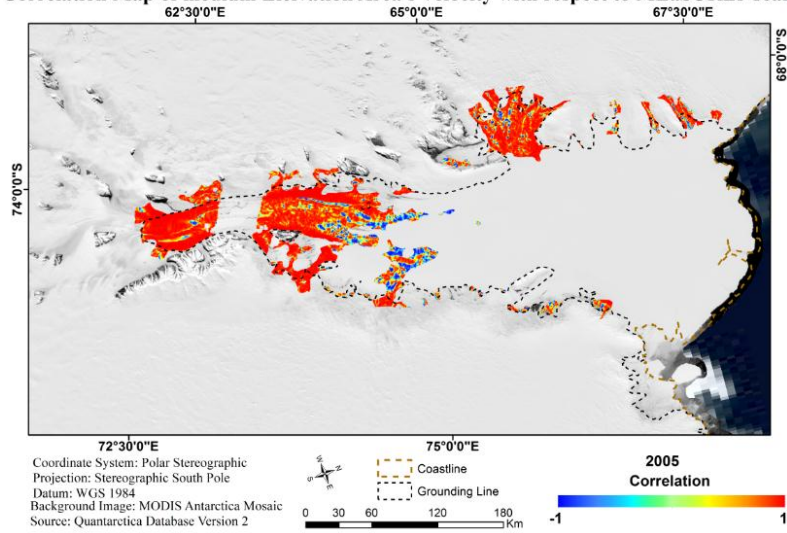
The values range from 0 to 150 m/a. This map is also generated using software called R Studio.



Correlation

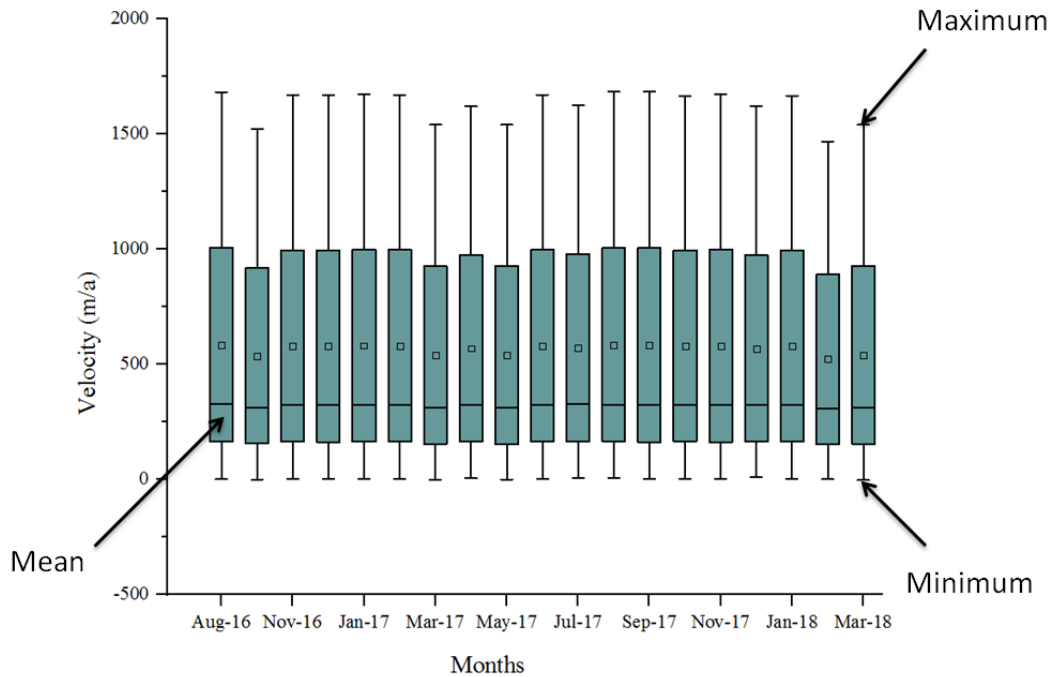
The generated velocity maps were correlated with respect to Stable Dataset generated, MEaSURES Ice Velocity at 450m, MEaSURES Yearly and GoLIVE data. The range is from -1 to 1. This map is generated using R Studio.

Correlation Map of medium Elevation Area's Velocity with respect to MEaSUREs Year

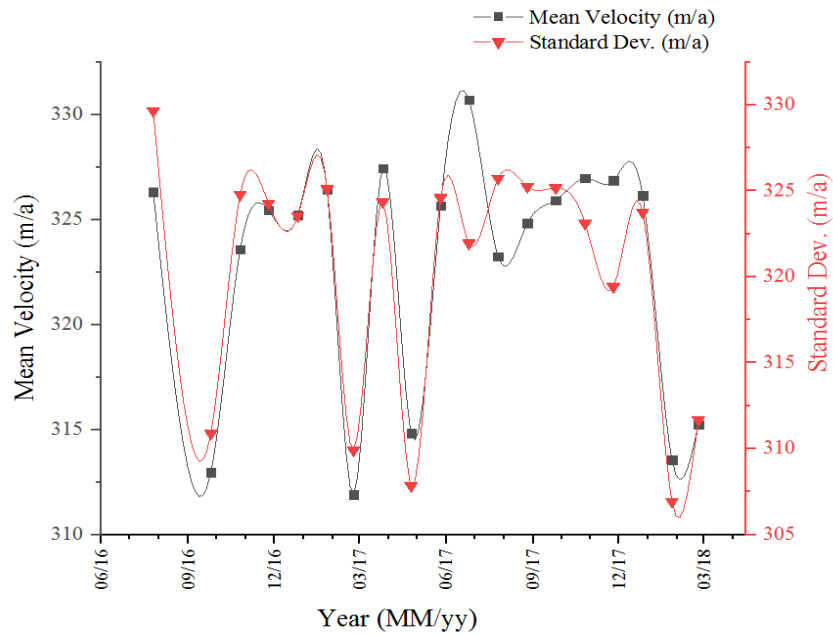


11. Discussion

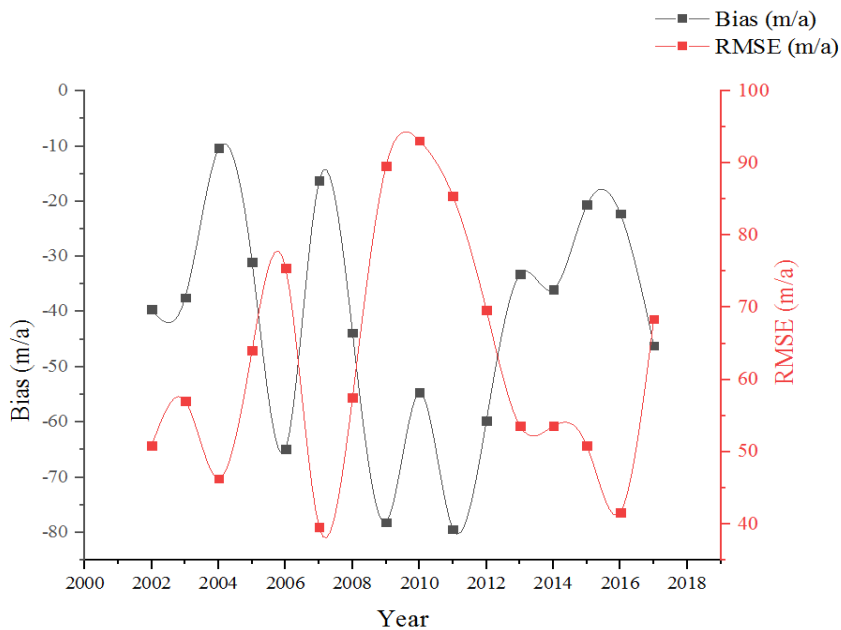
The velocity statistics was calculated with respect to the MEaSUREs Stable Data at 450m and MEaSUREs Yearly, GoLIVE, Stable Dataset generated. The BIA shapefile were used to extract velocity from the data to estimate the changes in velocity due to blue ice areas. The statistics were calculated with respect to the stable datasets. The velocity distribution is as shown below. The graph represents the minimum, maximum, mean and standard variation of the yearly and monthly velocities. The maximum velocity appears to be in the year 2017. The seasonal variations in very prominent in the graph plotted below.



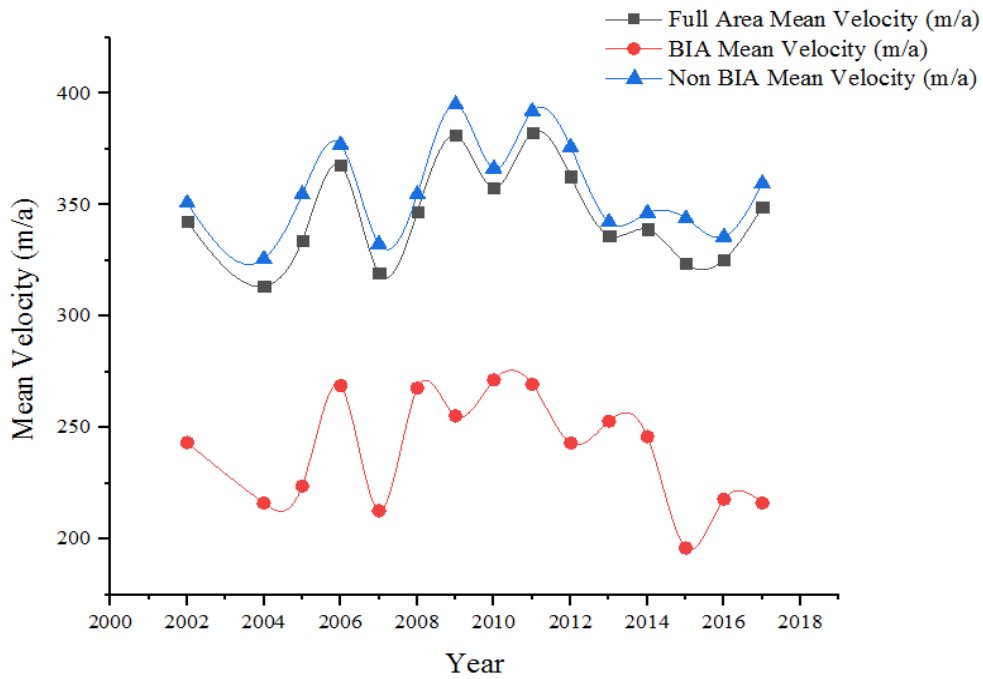
This graph represents the Mean Velocity and Standard deviation of the monthly velocity maps obtained.



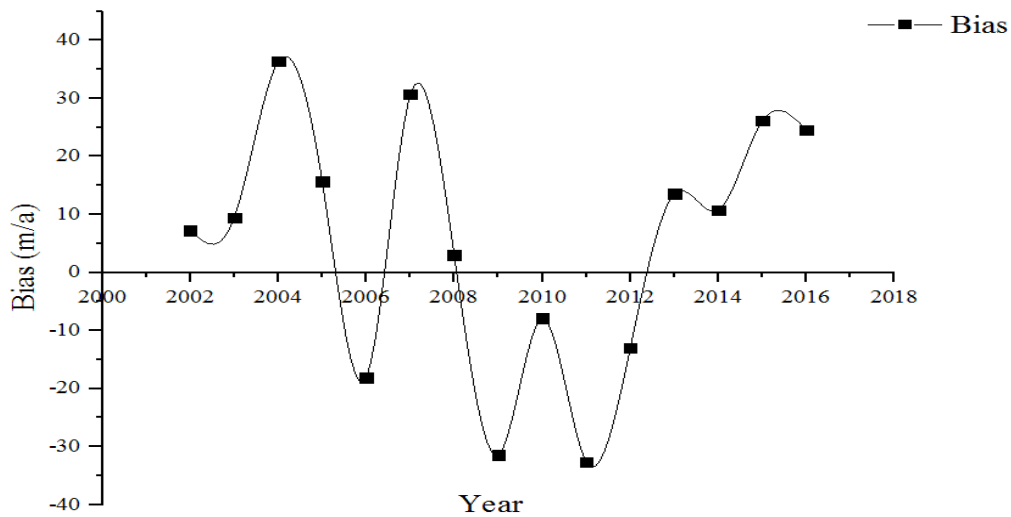
This map indicates the Bias and RMSE with respect to the Stable dataset generated over the time period 2001 to 2018.



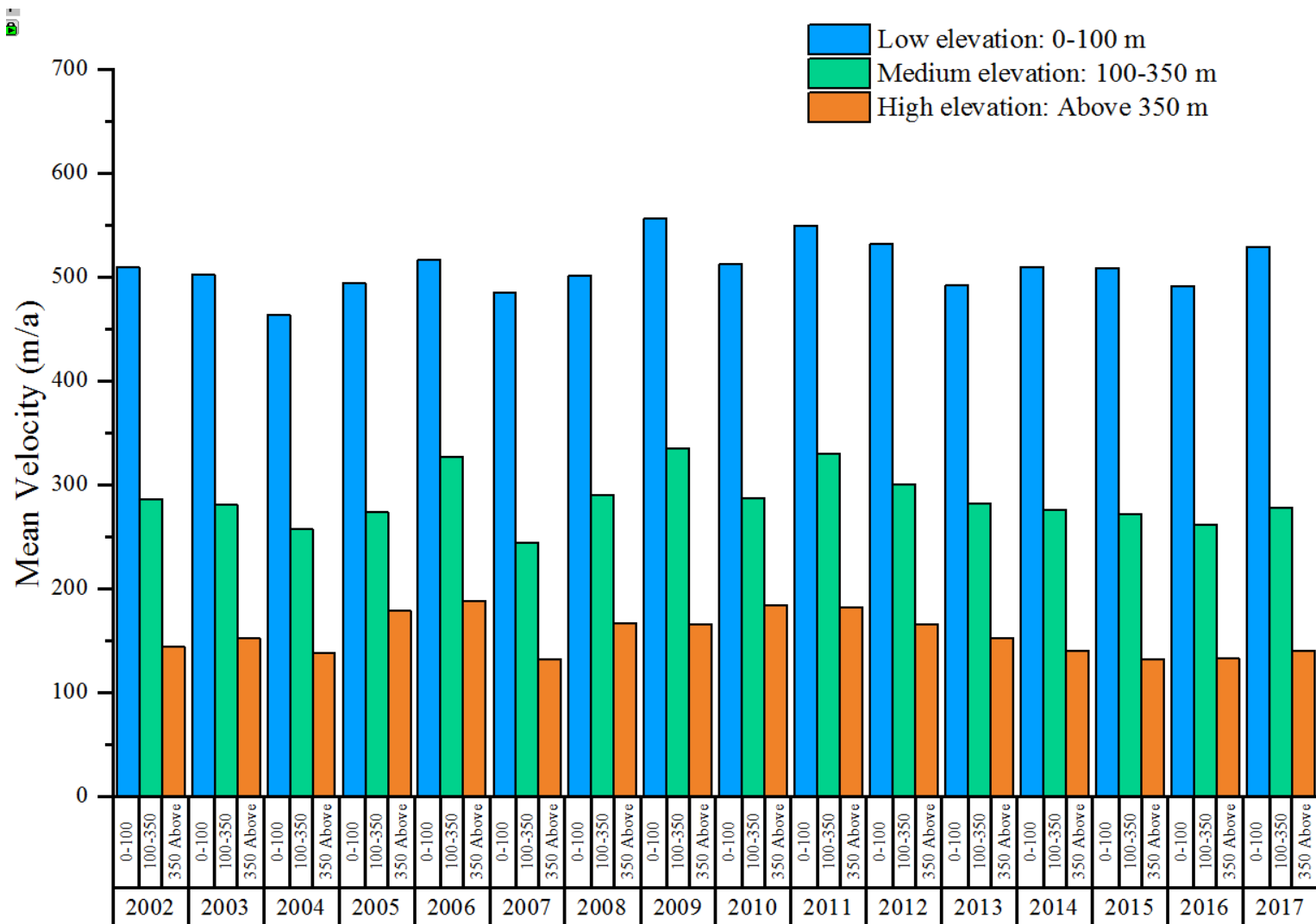
The next graph indicates the variation of BIA velocity with respect to the Non BIA areas and the whole area. It is clearly visible that BIA reduces the velocity of the area.



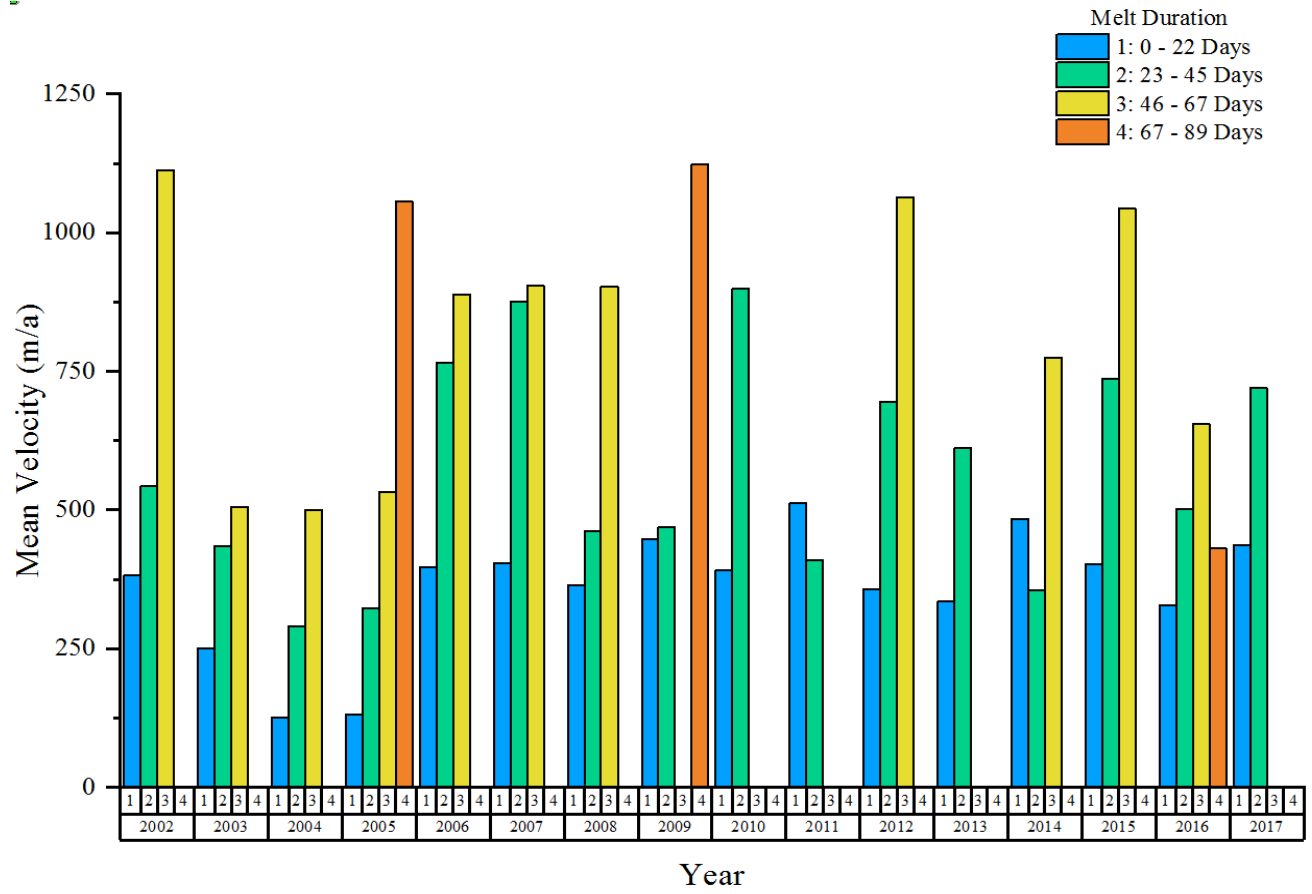
The variations in the yearly velocity were also calculated. The graph shown below is the shows the Bias of the period 2001 to 2017 with respect to 2017.



The areas of different elevation were categorized as High, Medium and Low and then again statistics were calculated to observe the elevation influence on the velocity change. It is clearly seen that velocity is higher in low elevation areas since these consist of ice shelf while the higher elevation zones are made up of grounded ice.



The contribution of melt to velocity was also observed. The melt varied proportionally to the velocity. The more the number of melting days or higher the melt duration, higher is the velocity in that region. Though studies actually show that melt is not a huge influencer of velocity.



12. Work and Cultural Experience

My journey in NCAOR may not be the first one in a research institute but obviously it has been the best one. The campus is beautifully situated on the coast.

The atmosphere in the Polar Remote Sensing lab was very good. The students were very friendly and from varied background. I got to learn a lot from them. The flexibility of the working hours was also a bonus for me. The enthusiasm of my guide is worth mentioning here. He was the one who motivated me to work on weekends and he too would be present on weekends. The work load kept me on my toes the whole time but at the same time never let me break down. The contribution goes to my guide too. I am very much interested to pursue research as my career. It helped me improve my skills of reading for long hours and also to improve my level of patience. When results were not as desired, I would sit for long hours only to sort out what went wrong. Even simple code errors would help to be careful the very next time. The work stations with very high RAM and all new softwares helped my carry out the work faster.

The cultural experience was amazing, staying with a Konkani family I came to know their culture. I was also lucky enough to attend the very famous Goa Carnival 2018.



13. References

- Anderson, B. (2011). Mountain glacier velocity variation during a retreat / advance cycle quantified using sub-pixel analysis of ASTER images, *57*(202), 197–207.
- Berthier, E., Vadon, H., Baratoux, D., Arnaud, Y., & Vincent, C. (2005). Surface motion of mountain glaciers derived from satellite optical imagery, *95*, 14–28. <https://doi.org/10.1016/j.rse.2004.11.005>
- Bhattacharya, A., Arora, M. K., & Sharma, M. L. (2015). Bhattacharya A , Arora MK , Sharma ML (2012) Improved Digital Elevation Model Creation using SAR Interferometry in Plane and Undulating Terrains . Himalayan Improved Digital Elevation Model creation using SAR Interferometry in plane and undulating terrains, *33*(January 2012), 29–44.
- Bothale, R. V, Rao, P. V. N., Dutt, C. B. S., Dadhwal, V. K., Larsen, C., & Vi, G. (2014). Spatio-temporal dynamics of surface melting over Antarctica using OSCAT and QuikSCAT scatterometer data (2001 – 2014), (Mi).
- Copland, L., Pope, S., Bishop, M. P., Shroder, J. F., Clendon, P., Bush, A., ... Owen, L. A. (2009). Glacier velocities across the central Karakoram, *50*(52), 41–49.
- Debella-gilo, M., & Kääb, A. (2011). LOCALLY ADAPTIVE TEMPLATE SIZES FOR MATCHING REPEAT IMAGES OF MASS Institute of Geosciences , University of Oslo , Oslo , Norway, (1), 4281–4284.
- Dehecq, A., Gourmelen, N., Trouvé, E., Dehecq, A., Gourmelen, N., & Trouvé, E. (2016). Deriving large-scale glacier velocities from a complete satellite archive : Application to the Pamir-Karakoram-Himalaya To cite this version : HAL Id : hal-01154166 Deriving large-scale glacier velocities from a complete.
- Documentation - Theory Interferometric SAR Processing. (2007), (November), 1–28.
- H. Jay Zwally¹, Waleed Abdalati, Tom Herring, Kristine Larson, Jack Saba¹, and K. S. (2002). Surface Melt-Induced Acceleration of Greenland Ice-Sheet Flow, *2002*(8).
- Heid, T. (2011). Deriving glacier surface velocities from repeat optical images.
- Hilmar, G., British, G., Survey, A., Marine, T., Model, I. S., Project, I., & Gudmundsson, G. H. (2014). Estimation of the surface displacement of Swiss alpine glaciers using satellite radar interferometry, (May).
- How to fill gaps in Landsat ETM images.* Retrieved from <https://yceo.yale.edu/how-fill-gaps-landsat-etm-images>
- How to convert Landsat DN's to Top of Atmosphere (ToA) Reflectance.* Retrieved from <https://yceo.yale.edu/how-convert-landsat-dns-top-atmosphere-toa-reflectance>
- Ian Joughin, Rol Kwok, M. F. (1996). Estitnation of ice-sheet motion using satellite radar interferotnetry : mmethod and error analysis with application to Hutnboldt Glacier , Greenland.
- Ian Joughin. (2002). Ice-sheet velocity mapping : a combined interferometric and speckle-tracking approach, 195–201.

- Ice sheets and glaciation*. Retrieved from <https://discoveringantarctica.org.uk/oceans-atmosphere-landscape/ice-land-and-sea/ice-sheets-and-glaciation/>
- IW GRD Resolutions - Sentinel-1 SAR Technical Guide - Sentinel Online*. Retrieved from <https://sentinel.esa.int/web/sentinel/technical-guides/sentinel-1-sar/products-algorithms/level-1-algorithms/ground-range-detected/iw>
- January 01, 1970 . *Geoinformatics Tutorial*. Retrieved from <http://geoinformaticstutorial.blogspot.in/2012/03/terrain-correction-of-sar-images-part-1.html>
- January 01, 1940. *National Snow and Ice Data Center*. Retrieved from <http://nsidc.org/data/nsidc-0082>
- Kenyi, L. W. (2003). Measuring rock glacier surface deformation using SAR interferometry, (1).
- Kumar, V., Venkataramana, G., & Høgdal, K. A. (2011). International Journal of Applied Earth Observation and Geoinformation Glacier surface velocity estimation using SAR interferometry technique applying ascending and descending passes in Himalayas. *International Journal of Applied Earth Observations and Geoinformation*, 13(4), 545–551. <https://doi.org/10.1016/j.jag.2011.02.004>
- Li, S., Benson, C., Gens, R., & Lingle, C. (2008). Remote Sensing of Environment Motion patterns of Nabesna Glacier (Alaska) revealed by interferometric SAR techniques, 112, 3628–3638. <https://doi.org/10.1016/j.rse.2008.05.015>
- Ligtenberg, S. R. M., Lenaerts, J. T. M., Broeke, M. R. V. A. N. D. E. N., & Scambos, T. A. (2014). On the formation of blue ice on Byrd Glacier , Antarctica, 60(219), 41–50. <https://doi.org/10.3189/2014JoG13J116>
- Liu, T., Niu, M., & Yang, Y. (2018). Ice Velocity Variations of the Polar Record Glacier (East Antarctica) Using a Rotation-Invariant Feature-Tracking Approach, (November 2002). <https://doi.org/10.3390/rs10010042>
- Lucchitta, B. K., Mullins, K. F., Allison, A. L., Survey, V. S. G., & Drive, N. G. (1993). Antarctic glacier-tongue velocities from Landsat images : first results.
- Luckman, A., Quincey, D., & Bevan, S. (2007). The potential of satellite radar interferometry and feature tracking for monitoring flow rates of Himalayan glaciers, 111, 172–181. <https://doi.org/10.1016/j.rse.2007.05.019>
- Mattar, K. E., Vachon, P. W., Member, S., Geudtner, D., Gray, A. L., Cumming, I. G., & Brugman, M. (1998). Validation of Alpine Glacier Velocity Measurements Using ERS Tandem-Mission SAR Data, 36(3), 974–984.
- Oza, S. R. (2015). Spatial – temporal patterns of surface melting observed over Antarctic ice shelves using scatterometer data, 27(February 2013), 403–410. <https://doi.org/10.1017/S0954102014000832>
- Pandit, P. H., Jawak, S. D., & Luis, A. J. (2018). Estimation of Velocity of the Polar Record Glacier , Antarctica Using SAR, 2(April), 1–6.

Retrieved from <https://landsat.gsfc.nasa.gov/landsat-data-continuity-mission/>

- Richard M. Goldstein, Herma Lingelhardt, B. K. and R. M. (1992). Satellite Radar Interferometry for Monitoring Ice-sheet Motion: Application to an Antarctic Ice Stream. *Journal of Glaciology*, 38(1), 1-12.
- Ruiz, L., Berthier, E., Masiokas, M., Pitte, P., & Villalba, R. (2015). First surface velocity maps for glaciers of Monte Tronador, North Patagonian Andes, derived from sequential Pléiades satellite images, *61*(229), 908–922. <https://doi.org/10.3189/2015JoG14J134>
- Scambos, T. A., Dutkiewicz, M. J., Wilson, J. C., Dettwiler, M., Columbia, B., & Bindschadler, R. A. (1992). Application of Image Cross-Correlation to the Measurement of Glacier Velocity Using Satellite Image Data, *186*(September 1991).
- Scherler, D., Leprince, S., & Strecker, M. R. (2008). Remote Sensing of Environment Glacier-surface velocities in alpine terrain from optical satellite imagery — Accuracy improvement and quality assessment, *112*, 3806–3819. <https://doi.org/10.1016/j.rse.2008.05.018>
- Sébastien Leprince. (2007). Automatic and Precise Orthorectification, Coregistration, and Subpixel Correlation of Satellite Images, Application to Ground Deformation Measurements, *45*(6), 1529–1558.
- Sood, S. Glacier Classification and Movement Estimation using SAR Polarimetric and Interferometric Techniques. *Journal of Remote Sensing*, 1(1), 1-12.
- Strozzi, T., Luckman, A., Murray, T., Wegmüller, U., & Werner, C. L. (n.d.). Glacier Motion Estimation Using SAR Offset-Tracking Procedures. *Support*. Retrieved from <http://www.harrisgeospatial.com/Support/Forums/tabid/2342/aft/4800/Default.aspx>
- Taylor, P. (2016). SAR Interferometry: Issues, techniques and applications. *Access details: Access*, (March). <https://doi.org/10.1080/01431169608948741>
- Th, I., America, S., & Patag, H. (1994). Flow of Glaciar Moreno, Argentina, from repeat-pass Shuttle Imaging Radar images: comparison of the phase correlation method with radar interferometry, (1).
- Werner, C. L. (1988). Satellite Radar Interferometry: Two-Dimensional Phase Unwrapping, (October). <https://doi.org/10.1029/RS023i004p00713>
- Zhou, C., Zhou, Y., Deng, F., Ai, S., Wang, Z., & Dongchen, E. (2014). Seasonal and interannual ice velocity changes of Polar Record, *55*(66), 45–51. <https://doi.org/10.3189/2014AoG66A185>